Aerodynamics of Endwall Contouring with Discrete Holes and an Upstream Purge Slot Under Transonic Conditions with and without Blowing

Dorian Matthew Blot

Thesis submitted to the Faculty of
Virginia Polytechnic Institute and State University
in partial fulfillment of the requirements for the degree of

Master of Science
In
Mechanical Engineering

Srinath V. Ekkad
Wing F. Ng
Walter F. O'Brien Jr.

12/6/2012
Blacksburg, VA

Keywords: Gas Turbines, Transonic Cascade, Aerodynamics. Heat Transfer, Film Cooling, Upstream Purge Slot, Discrete Hole Cooling, Endwall Contouring

Aerodynamics of Endwall Contouring with Discrete Holes and an Upstream Purge Slot Under Transonic Conditions with and without Blowing

Dorian Matthew Blot

Abstract

Endwall contouring has been widely studied as an effective measure to improve aerodynamic performance by reducing secondary flow strength. The effects of endwall contouring with discrete holes and an upstream purge slot for a high turning (127°) airfoil passage under transonic conditions are investigated. The total pressure loss and secondary flow field were measured for two endwall geometries. The non-axisymmetric endwall was developed through an optimization study [1] to minimize secondary losses and is compared to a baseline planar endwall. The blade inlet span increased by 13 degrees with respect to the inlet in order to match engine representative inlet/exit Mach number loading in a HP turbine. The experiments were performed in a quasi-2D linear cascade with measurements at design exit Mach number 0.88 and incidence angle. Four cases were analyzed for each endwall – the effect of slot presence (with/without coolant) and the effect of discrete holes (with/without coolant) without slot injection. The coolant to mainstream mass flow ratio was set at 1.0% and 0.25% for upstream purge slot and discrete holes, respectively. Aerodynamic loss coefficient is calculated with the measured exit total pressure at 0.1 C_{ax} downstream of the blade trailing edge. CFD studies were conducted in compliment. The aero-optimized endwall yielded lower losses than baseline without the presence of the slot. However, in presence of the slot, losses increased due to formation of additional vortices. For both endwall geometries, results reveal that the slot has increased losses, while the addition of coolant further influences secondary flow development.

To my Family & Adelaide

Acknowledgements

I am indebted to both Dr. Srinath Ekkad and Dr. Wing Ng for their continuous guidance. Their critiques, discussions, and applicable knowledge aided in my understanding in the course of this project. I especially want to extend my thanks to Dr. Ekkad for his faith in me and allowing me this opportunity, I am eternally grateful. I would also like to thank Andrew Lohaus and Michael Crawford from Siemens for their funding and their valued suggestions and discussions during my time on this project. Thank you to Dr. O'Brien, my committee member, for some great learning opportunities.

Thank you to all my friends for the times we have had here at Virginia Tech. I would like to thank my lab mates, particularly Megan Dove Thompson, Christopher LeBlanc, Justin Lamont, Bonaventure Nunes, Jaideep Pandit, Patrick Seiler, Sridharan Ramesh, and Arnab Roy for the fun times we have had and especially the open conversations that assisted all of us in our research and studies. Thank you for the memories and your friendships.

A special thanks goes to, Jacob Delimont, Bonaventure Nunes, Jaideep Pandit, Patrick Seiler, Sridharan Ramesh, Colin Reagle, Arnab Roy, and Song Xue. Without your knowledge, experience and your time to give a helping hand, the timely completion of this project would not have been possible. Most of all, Arnab Roy, thank you for everything. Your support and friendship was instrumental and will always be cherished.

Finally, I would like to thank my parents, my brother, and Adelaide Marciano for their guidance and inspiration. Without your loving support, I certainly would not be who I am today. Thank you!

Table of Contents

List of Figures

List of Tables

List of Equations

Nomenclature

C_{ax}	Axial chord length
C_p	The specific heat capacity at a constant pressure
HTC	Heat transfer coefficient (h)
IP	Increased pitch
M_{iso}	Isentropic Mach number
MFR	Coolant to Mainstream Mass Flow Ratio
p_{01}	Inlet Total Pressure measured 0.45 $\mathbf{C_{ax}}$ upstream of the cascade
p_{02}	Exit Total Pressure
p_{s2}	Exit Static Pressure
p_{0in}	Pitchwise average stagnation pressure at inlet midspan
p_0	Local stagnation pressure
p_s	Local static pressure
p_{sexit}	Static Pressure
Pt_{exit}	Exit total pressure
Pt_{in}	Inlet total pressure
PS	Pressure Surface
SP	Short Pitch
SS	Suction Surface
T_0	Stagnation temperature
T, T_s	Static temperature
T_t	Total temperature

T_∞	Mainstream Temperature
W_ω	Uncertainty in Loss Coefficient

Greek Letters

γ	Ratio of Specific Heats $\frac{C_p}{C_v}$
ρ	Density
ω	Loss coefficient $\frac{p_{0,in}-p_{0,exit}}{p_{0,exit}-p_{s,exit}} = \frac{p_{01}-p_{02}}{p_{02}-p_{s2}}$

Chapter 1: Introduction

In an effort to increase performance and efficiency with higher turbine inlet temperatures, while restricting emission levels under stringent limitations, presents challenges to gas turbine engineers. Modern gas turbines have highly loaded airfoils, which are advantageous by reducing the number of blades per stage, therefore lowering weight and cost. However, advanced cooling strategies are required to meet the increased heat load to the passages from mainstream hot gas. There are many methods employed to counteract these temperatures. The two that will be discussed here with be upstream purge flow and endwall discrete hole cooling.

Increased airfoil loading does come with economic benefits however it could result in higher secondary losses. Secondary flows in turbine passages arise due to the complex interaction between the mainstream inlet boundary layer and the airfoil/endwall junction at the blade leading edge. The upstream boundary layer thickness along with the airfoil turning angle influences the strength of the secondary flows observed near the endwalls. The secondary flows are responsible for the formation of several vortices along the passage which increase the aerodynamic losses. The overall turbine efficiency can be greatly affected by secondary flows. Secondary flows result in stagnation pressure loss contributing to a major portion of the total losses. Furthermore, secondary flows create non-uniform exit flow conditions decreasing the performance of subsequent stages. However, it has been shown that the increase in airfoil loading has a significant impact on secondary flow strength [2-5].

Due to turbine assembly, several gaps exist between the alignment of the stationary and rotating parts within the engine. The hot gas can be detrimental to the engine if it is allowed to pass into these gaps causing thermal fatigue. In order to prevent the ingestion of hot gas, high

pressure air from the compressor is bypassed through these leakage slots to act a seal. The pressure difference between the cooling air and the mainstream prevents the hot gas from entering the cavities as well as providing film cooling for turbine endwall surfaces.

The leakage flows can further intensify the passage vortex increasing the aerodynamic losses. Endwall contouring is a widely studied practice as a means to effectively control secondary flow strength and direction, with the intentions to minimize secondary flow losses in turbine passages. Endwall geometries or surface profiling can be classified in two categories, axisymmetric contouring and non-axisymmetric contouring. Axisymmetric contouring is where the profile is dependent on axial coordinates, while non-axisymmetric contouring has endwall shape that is three dimensional and designed as several peaks and valleys along the endwall. It has been observed that non-axisymmetric endwall profiling tends to yield more beneficial reductions in total pressure loss than an axisymmetric design.

1.1 Literature Survey

Blair [6] was one of the earliest to report reduced heat transfer due to upstream film coolant injection and suggested the possible impact of the coolant on the flow. He found that the transition zone for the endwall boundary layer could be affected by the upstream slot. He further studied this by using a smooth geometry with a trip wire to measure the effects on the boundary layer. Results indicated that the slot and coolant injection both acted to promote transition within the boundary layer.

There have been many studies on secondary flow losses that are encountered in a turbine blade passage. The work of Armaly et al. [7], was a fundamental study into the effects of a backward facing step. There was no leakage flow considered here or even a cascade experiment.

They used a laser Doppler velocimeter (LDV) technique in order to measure the velocity distribution and reattachment lengths for laminar, transitional, and turbulent flows downstream of a single backward facing step mounted in a 2D channel. Aside from the expected primary recirculation zone attached to the backward facing step, they observed that the reattachment length was a function of the Reynolds number and additional regions of flow separation downstream of the step and on both sides of the channel test section developed.

Heat and mass transfer experiments along with flow visualizations were performed by Papa et al. [8] in a linear cascade with an upstream injection slot. The oil-dot flow visualization confirmed that with coolant injection created a recirculation zone upstream of the leading edge of the airfoil and the growth of the passage vortex was altered. The secondary flow caused the flow exiting the slot to be pulled to the blade suction side and pushed along its surface. At the highest blowing ratio of 1.5 the coolant had enough momentum to change the flow structure so that the coolant was able to avoid entrainment into the passage vortex and travel closely along the blade profile.

There have been studies by researchers into the effects that a flush slot, backwards facing slot, or a forward facing slot. Colban et al. [9] mentioned that slot flow interaction with turbulent mainstream influences the total pressure profile seen by the blade passages, therefore manipulating the secondary flow development. The tests performed were for a nozzle guide vane with a realistic combustor exit profile. Utilizing a Kiel probe to measure the stagnation pressure and LDV, the inlet flow conditions were measured. From this and the adiabatic effectiveness values obtained from their infrared camera they were able to determine that the difference in total pressure from the fluid above and below the backward facing step caused ingestion into the slot. Thereby increasing the slot flow decreased the driving potential between the main gas and

the coolant. In the Part II of the paper by Colban et al. [10] evaluated the effect of increasing slot flow on secondary flow development. The passage with the upstream film cooling slot showed a secondary flow pattern with a significantly different flow field than expected for an approaching two-dimensional turbulent boundary layer. As a result the passage vortex became stronger for the slot configuration while the suction side leg of the horseshoe vortex diminished in strength. As a result counter-rotating vortex also appeared above the passage vortex. When cooling was increased, a higher total pressure exited the slot decreasing the strength and size of the passage vortex and increasing the strength of the counter–rotating vortex.

Blanco et al. [11], also looked into the effects of a backward and forward facing step with and without leakage flow and found similar result to Colban et al. [9]. The forward facing step produced stronger endwall flows compared to the backward facing step. They also found that the backward facing step under certain flow conditions yielded lower losses than the flat endwall. The slot design weakened the strength of the suction side corner vortex and passage vortex while the trailing shed vorticity is larger. However, with the addition of leakage flow causes the loss cores for the corner and passage vortex to increase, while migrating closer towards the midspan. A flow simulation was also performed that showed that the inlet endwall boundary layer rolls up into three discrete vertical structures with the same vertical sense as the passage vortex. These vortices later are swept into the passage vortex. Biesinger and Gregory-Smith [12] as cited by Minking Chyu [13] utilized upstream slot injection in order to control secondary flows. They too found that the effects of low velocity bleeding induces more losses and strengthens the secondary flows, through the thickening of the boundary layer. Alternately, high velocity injection re-energized the boundary layer and weakened the passage vortex.

The work presented by Paniagua et al. [14], was an investigation of hub enwall cavity flow ejection into the mainstream utilizing a time-averaged and time-resolved measurements in a transonic turbine stage. For a positive 1.5% ejection there was an increase of 6% in exit static pressure. In the computational study by Knost et al. [15] a three-dimensional slot design with endwall coolant holes were analyzed. It was found that the slot location could cause the earlier development of the horseshoe vortex. By having the slot centerline further upstream produced a more uniform pressure variation across the endwall. Gao et al. [16] utilized delta winds to produce upstream vortices. It was found that the strength and direction of the upstream vortices can be detrimental to slot cooling and thus influencing the passage vortex. The pressure sensitive paint (PSP) data showed there was a non-uniform pressure distribution along the exit of the slot with higher pressure exiting near the pressure side of the passage. The pressure at the midspan matched closely with the pressure of the platform near the PS whereas the pressure on the SS was higher, decreasing the pressure differential across the passage.

The effects of endwall contouring in turbine passages are readily available in literature. Morris et al. [17] performed low velocity tests on linear cascades with varying endwall geometries. They published one of the first studies on advantages of endwall profiling and reported 25% overall loss reduction. Dossena et al. [18] found that the vortex structures are strongly affected by the endwall contouring, presented improvements of 0.49 for overall mass averaged losses using a contoured endwall over a planar endwall. The contraction with the profiled endwall inhibits the formation of a stronger passage vortex and its growth towards midspan due to local acceleration and deflection of the suction side boundary layer. Duden et al. [19] conducted experiments using axisymmetric endwall for high turning airfoils (~100°), but didn’t yielded any major improvements in aerodynamic loss reduction. Experiments performed

by Burd and Simon [20] suggests that contoured endwall is able to control the secondary flow better compared to a flat endwall and explained near endwall flow behavior in view of boundary layer thinning and streamwise acceleration within the passage. Further studies by Hartland et al., Nagel et al., Prainser et al., Ross et al., and Snedden et al. [21-25] have been conducted by several researchers investigating the effect of endwall contouring on aerodynamic performance of turbine passages, however, all of these papers report results at low exit Mach numbers and Reynolds number contrary to as encountered in modern HP turbines.

There have only been limited studies that investigate the effects of endwall contouring at high exit Mach number or transonic operating conditions. Kopper et al. [26] performed experiments on an axisymmetrically contoured endwall at an exit Mach number 0.85 on a low turning angle low aspect ratio vane and demonstrated a 17% reduction in mass averaged losses. Taremi et al. [27] concluded that the at transonic operating conditions for high turning angle airfoils, reduction in losses are negligible using a contoured endwall.

The work by Friedrichs et al. and Kost et al. [28, 29] had the most similar test set up, where they performed experiments in a high speed linear cascade for and upstream slot and endwall coolant holes. Friedrichs et al. performed studies for inlet Mach number of 0.8 to 2.4, while Kost et al. used and inlet Mach number of 1.0. Friedrichs et al. found that the secondary flow structure is not affected by coolant injection downstream of the separation line on the endwall. However, coolant injection upstream of the separation line can alter the secondary flow reduce its losses. Results also showed, that reductions in aerodynamic losses can be had with film hole placement in high static pressure regions. One such case yielded a 0.3% reduction in losses. Similar to previously discussed reports, Kost et al. found that the passage vortex and the endwall cross flow is reduced through coolant injection from the holes and the slot. The

intensification of the horseshoe vortex can occur due to slot ejection at the saddle point. Overall the net secondary losses increased with coolant ejection. Recently, the aerodynamic performance at transonic speeds for a linear cascade with a diverging endwall at design and off design conditions was published by Abraham et al. [30]. In their work they measured the loss coefficients at both 0.1 C_{ax} and 1.0 C_{ax} from the trailing edge of an airfoil. They concluded that the secondary loses would increase as a result of increasing the pitch by 25% using the same blade profile.

Characterizing the endwall flow structures and in-depth understanding of secondary losses has been an active area of research in the past two decades due to their effects on turbine performance. The present study is a continuation and further development of Abraham et al [30] to incorporate effects of leakage flow coupled with non-axisymmetric endwall contouring. A detailed study of pressure loss variations at a plane 0.1 axial chord downstream of the trailing edge of a high turning (~ 127°) airfoil for both, planar and contoured endwalls, in presence of leakage slot and with discrete holes are presented for transonic operating conditions. The upstream leakage slot is tested at 0% and 1% MFR, whereas the discrete holes are tested at both 0% and 0.25% MFR when there is no slot leakage flow. The loss measurements are investigated at a design exit Mach number (0.88) and design incidence angle. The pressures measured previously by Santosh et al. [30] in case of without any upstream slot were manipulated using a different loss coefficient definition and have been presented again here for comparison to highlight the influence of the slot itself. To knowledge of the author, no experimental studies are available in open literature that investigates the effect of endwall contouring on aerodynamic performance of high turning airfoils in presence of upstream leakage flow.

Chapter 2: Test Facility, Experimental Set Up, Data Acquisition and Post-Processing

2.1 Test Facility

A schematic of Virginia Tech's transonic cascade wind tunnel is shown in Figure 2.1. The wind tunnel is a blow down facility capable of a twenty second run time. The air supply is pressurized by a four-stage Ingersoll-Rand compressor and stored in large outdoor tanks. The maximum tank pressure used for transonic tests is about 2068 kPa (300psig). A control valve is used to regulate the flow from the tanks to the test section. During a run, the upstream total pressure is held constant by varying the opening of a butterfly valve controlled by a computerized feedback circuit. There is additionally a safety valve upstream of the control valve to start and stop the tunnel. The airfoil isentropic exit Mach number is varied by changing the upstream total pressure.

$$M_{iso} = \sqrt{\left[\left(\frac{p_{01}}{p_{s2}}\right)^{\frac{\gamma-1}{\gamma}} - 1\right]\frac{2}{\gamma-1}} \qquad \textbf{Equation 2.1}$$

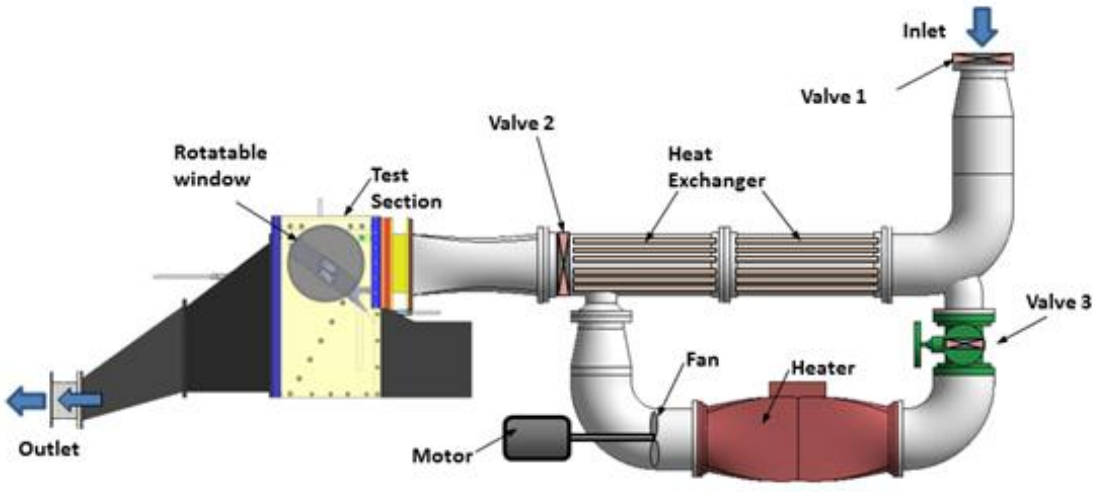

Figure 2.1: Virginia Tech transonic cascade wind tunnel facility

The airflow through the cascade is controlled by three valves, one at the inlet of the cascade, second valve just before test section inlet and the third valve in the heater section as shown in Figure 2.1. The first and the second valve remain open during the aerodynamic measurements while the third one remains closed allowing the air to flow directly from the inlet to the test section. For the heat transfer experiments, valves one and two are initially kept closed and the third valve is kept open. Air is circulated through the heater and heat exchanger, where the heated air heats the copper tubes. When the heat exchanger reaches a specified magnitude, in this case ~212 ^{o}F, the third valve is closed and the other two valves are opened. The passing air from the inlet gets heated through the heat exchanger just before it meets the test section.

2.2 **Test Section**

The cascade test section, as shown in Figure 2.1 consists of five airfoils resulting in four passages, with a controlled bleed flow above the first airfoil. This passage design is referred to as Increased Pitch (IP), in order to differentiate between results previous presented in the dissertations of by Santosh Abraham and Kapil Panchal [31, 32]. The airfoils are mounted on a rotatable window, which allows for changes in incidence angles as and when required. These experiments were all performed at a design incidence angle; therefore the cascade angle was fixed. Airfoil three from top is considered as the center airfoil of the linear cascade. The 3rd passage from top is the passage of interest during the experiments to ensure the periodic flow conditions. A headboard, positioned upstream of the cascade is instrumental in controlling the incoming flow by preventing an induced incidence angle effect on the leading edges of the airfoils. The headboard is used to create and control a flow bleed that prevents the flow from turning prior to reaching the leading edge of the airfoils. Uniform inlet flow conditions can be achieved by careful adjustment of the headboard angle which aids in maintaining uniform and

periodic flow through each airfoil passage and ensuring that the flow angle gradient ahead of the cascade is zero. A slot on the turntable window, located at 0.45 C_{ax} upstream of the cascade, is used to measure the turbulence and velocity distribution at the inlet of the cascade. It is also used to measure inlet total pressure at midspan which is used as a reference total pressure for isentropic Mach number calculation. Tailboards are positioned at the top airfoil and bottom airfoil trailing edges to help guide the flow.

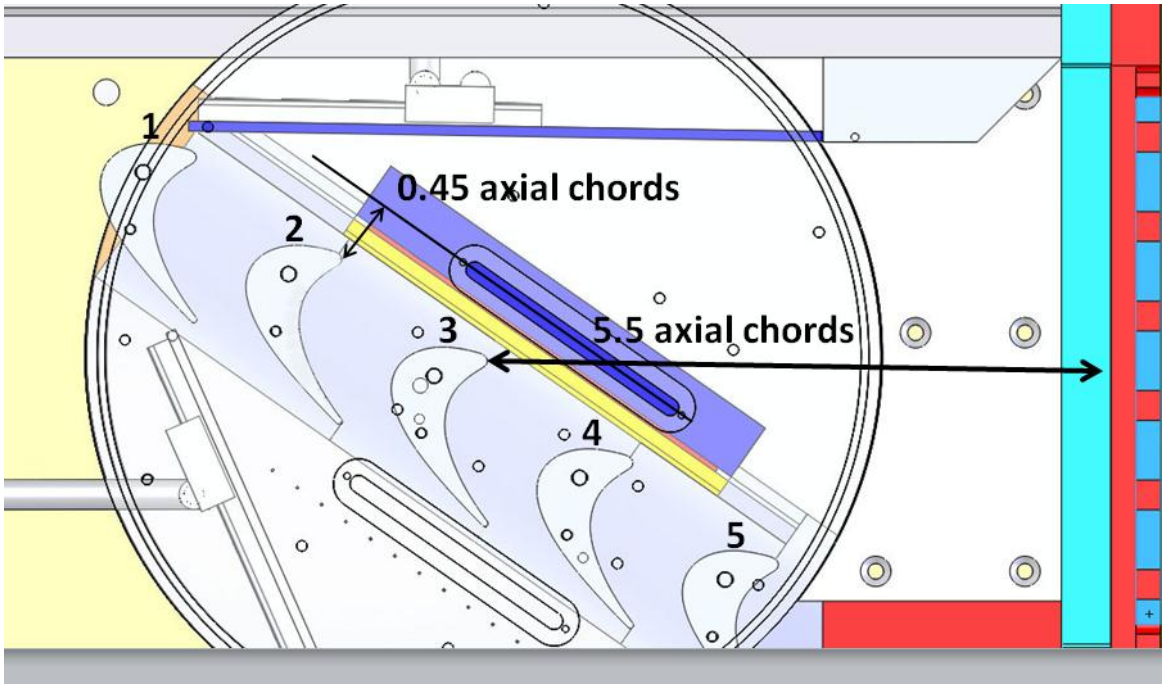

Figure 2.2: Test section

In the attempt to obtain real engine representative ratio of inlet Mach number to exit Mach number airfoil and near end wall loading, the exit span was increased relative to the inlet span resulting in one end wall diverging from inlet to exit at a 13° angle, which simulates the required leading edge loading in a quasi-2D cascade. The airfoil span increases by about 16% linearly in the axial direction, from inlet to exit of the cascade as shown in Figure 2.3.

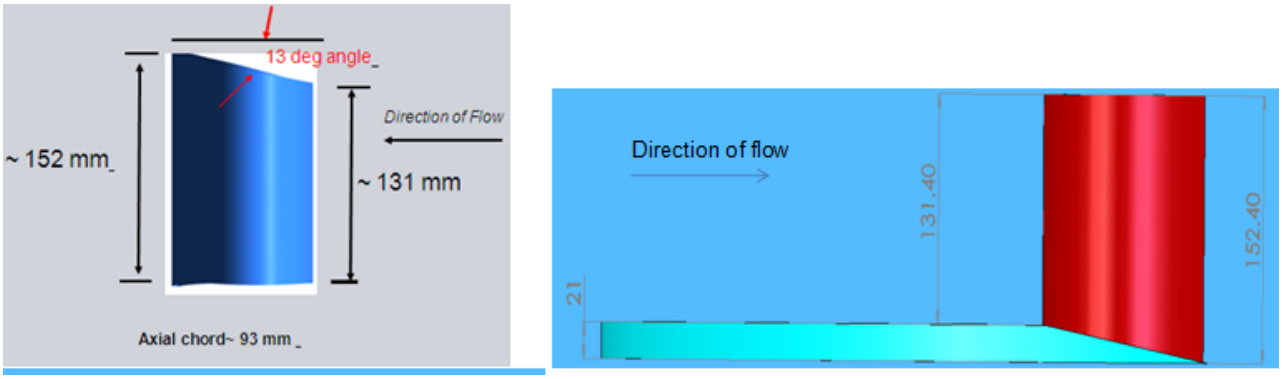

Figure 2.3: Change in inlet span relative to exit span

Siemens Energy Inc. provided the endwall designs to be investigated. The first one was a flat angled endwall and the second was a contoured geometry designed to minimize secondary aerodynamic losses also referred to as the aero-optimized endwall shown in Figure 2.4. The contoured endwall has a peak region starting near the leading edge pressure side that extends towards mid passage and a trough region along the suction side of the airfoil from ~0.2 normalized axial chord up to near the trailing edge. Details of the design process of these endwall geometries can be found in Panchal et al [1].

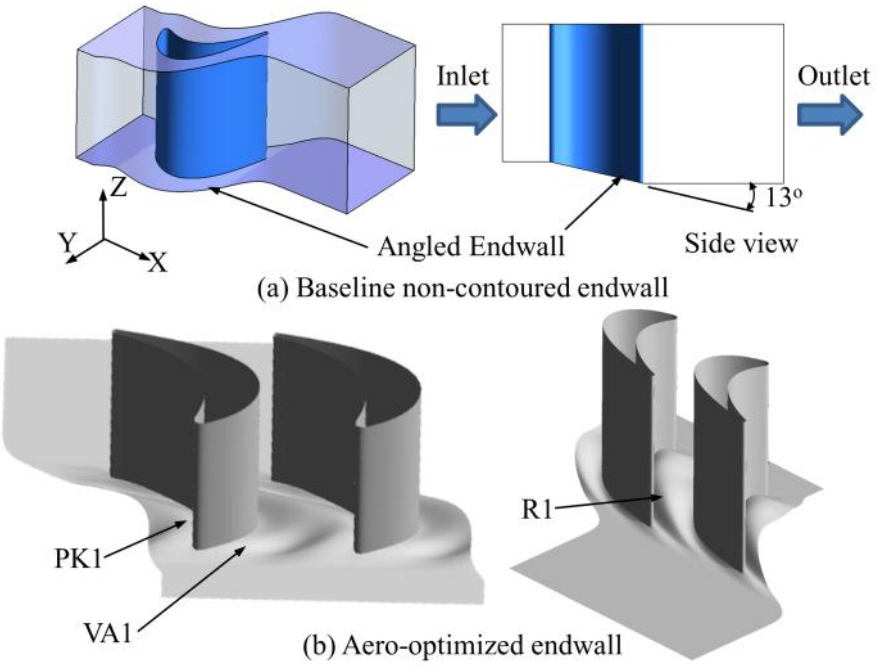

Figure 2.4: Endwall designs

2.3 Test Section Details

2.3.1 Upstream Leakage Slot Design

Figure 2.3 presents the upstream slot designed utilized in both endwall geometries. The upstream purge slot was placed ~ 0.3 axial chord distance upstream of the leading edge of airfoil. Internal features of the upstream leakage slot are also detailed. The coolant path through the slot is shown in Figure 2.3 (b) for clarity. Siemens' original design had angled vanes instead of straight vanes as shown Figure 2.3 to produce coolant swirl before exiting into the mainstream.

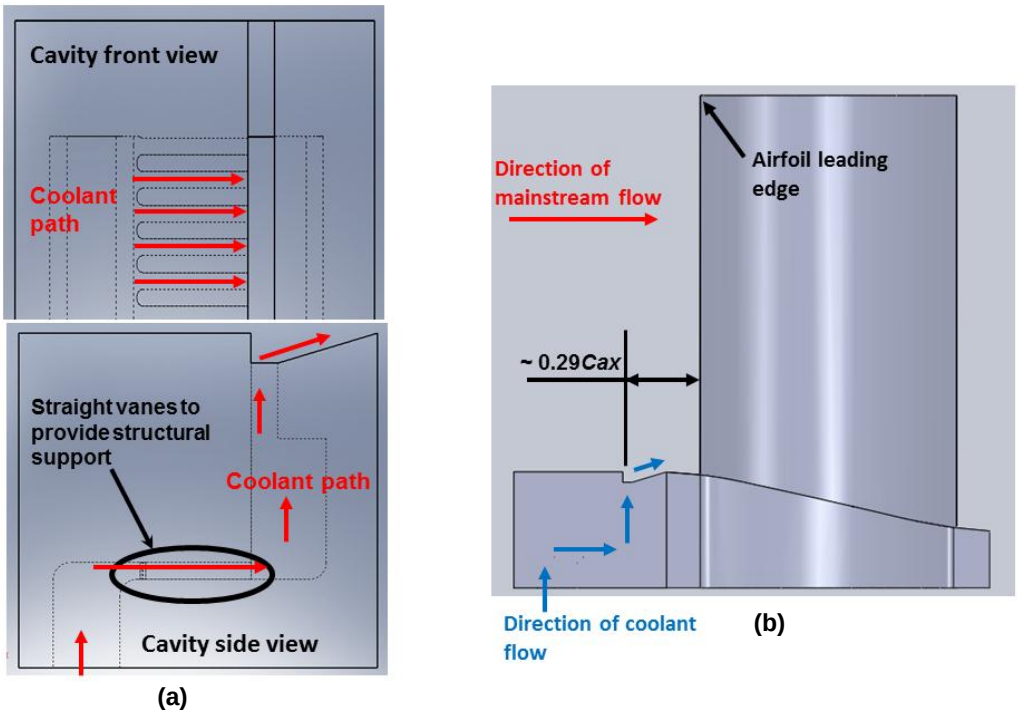

Figure 2.5: Upstream slot design – (a) Internal details, (b) slot location

After testing, it was found out that, the angled vanes created huge flow stagnation zones inside the cavity near the exit and therefore, outgoing coolant flow throughout the length of the slot was highly non-uniform. The swirl vane design was suitable for an annular cascade, but due to space limitation in our linear cascade straight parallel vanes were necessary in order to obtain

uniform flow. Aside from the vane angle modification all spacing and other dimensions were kept identical. The straight vane design results in no the coolant flow swirl, but ensures exit flow uniformity and provides structural support to the cavity. The slot length was optimized to be ~ 2.57 pitch distance equally spaced around the leading edge of the center airfoil keeping in mind to minimize wall effects on the exit flow; maximum coolant mass flow rate capacity and making sure uniform slot exit velocity can be maintained throughout the measurement passage. Figure 2.6 shows the center part (includes passage 2 and 3 and airfoil 3 and 4) of baseline and AO endwall geometry with upstream leakage slot.

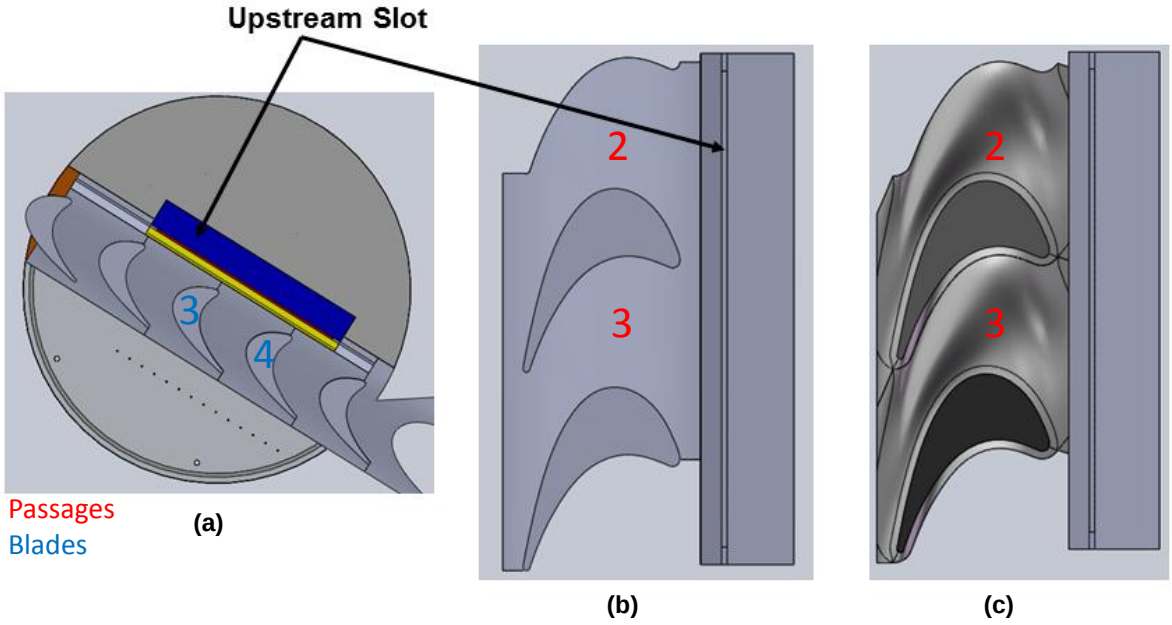

Figure 2.6: (a) Cascade with upstream slot Baseline endwall, (b) Baseline center part with upstream slot, (c) AO endwall center part with upstream slot

2.3.2 **Discrete Hole Design**

Siemens Energy Inc. also provided the design for the endwall film cooling discrete holes. All the film cooling holes are cylindrical in shape with a diameter of 1.2mm. The hole angles were based on specific coolant requirements at corresponding locations. The location of the array

of holes as shown in Figure 2.7 starts just after the leading edge from pressure side of the airfoil and extends up to ~ 0.5 axial chord length along the passage.

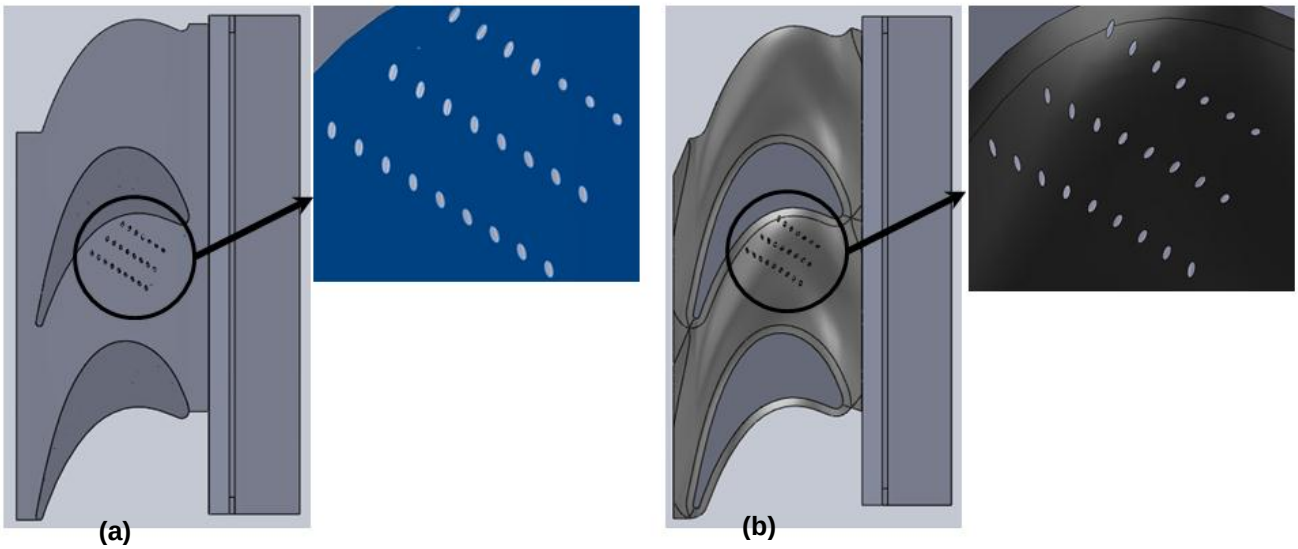

Figure 2.7: Discrete hole geometries on (a) baseline and (b) AO endwall

There are three rows of coolant holes, where the first, second and third row consists of 7, 8 and 9 holes respectively. An individual row starts near the airfoil pressure side endwall junction and ends near mid passage. The length to diameter (L/D) ratio of all the holes were ~ 5 to simulate actual engine representative hole designs. In order to keep such a small L/D ratio for both endwall geometries, the coolant plenum was embedded inside the endwall by making a cavity inside the geometry. The hole inlet surface profile was made the same as the external endwall surface as shown in Figure 2.7 by offsetting the endwall surface. Hence, the coolant after entering into the cavity from external plumbing system flows into the coolant holes. The coolant cavity ensures proper mixing of the coolant stream and coolant temperature measurement was also performed inside the cavity just before the inlet of the cooling holes. The physical coordinates of the hole locations on endwall are identical and were based on cooling

requirements of high heat transfer zones along the passage horse-shoe vortex flow path for both the baseline and AO endwalls in mind.

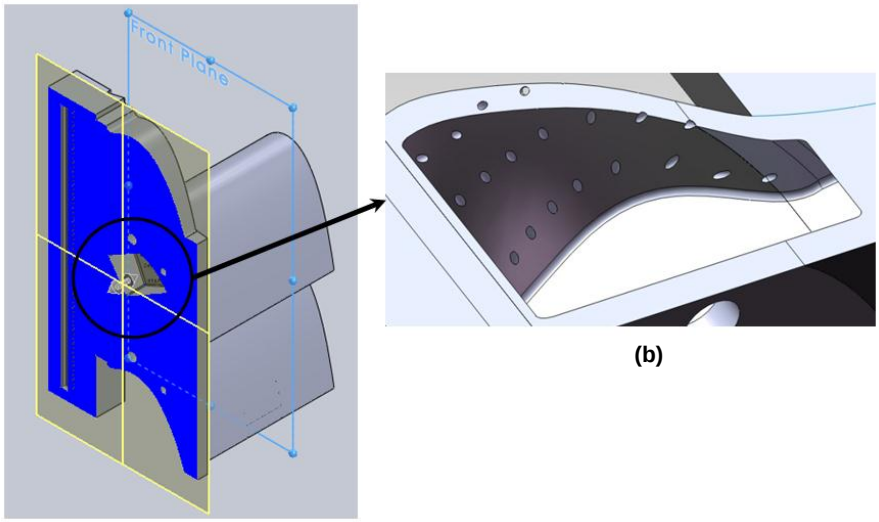

Figure 2.8: Discrete hole coolant cavity (a) section plane, (b) coolant cavity inside view

2.4 Coolant System

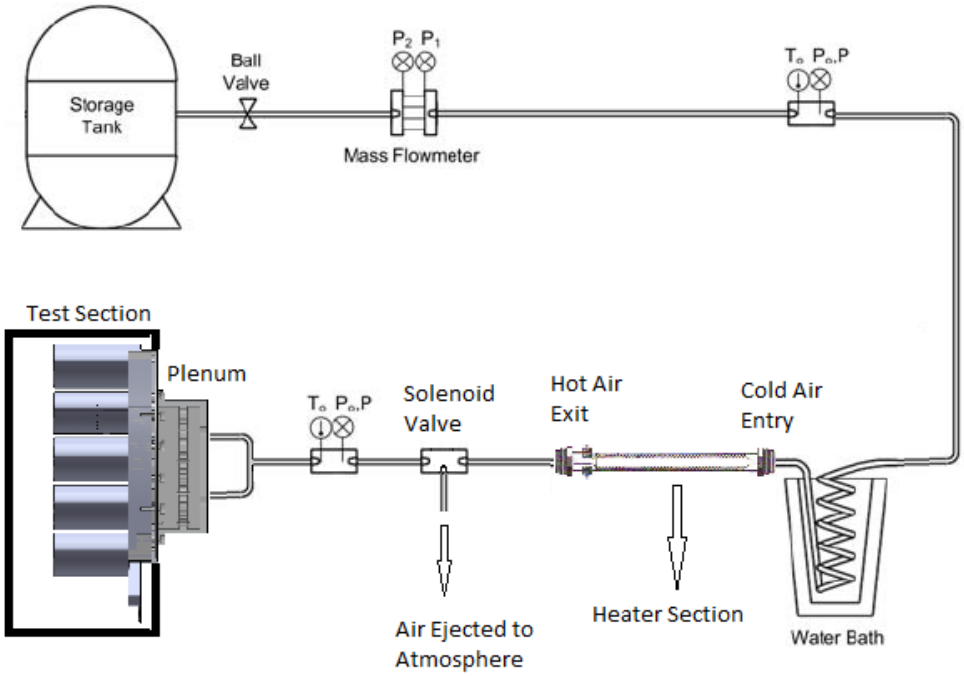

Figure 2.9: Coolant system set up

Figure 2.9 represents a schematic of the coolant system set up. A shop compressor would charge the high pressure storage tank to provide the coolant supply during the experiments. The coolant system consisted of globe valves for mass flow control, solenoid valves for diverting the coolant flow away and towards test section at appropriate times, orifice meters for mass flow rate measurement, and thermocouples for coolant temperature measurement. For heat transfer experiments as will be described later, the coolant air was required to be heated up or chilled as necessary. Therefore, for "cold coolant" runs an ice water bath was used just to chill the coolant and for "hot coolant" runs, the coolant was heated using a heating cord wrapped around coolant plumbing with a temperature controlling device.

2.5 Aerodynamic Measurements

In this section, the procedures taken to establish the test section flow conditions for upstream flow uniformity, passage flow periodicity, turbulence intensity, and isentropic Mach number will be discussed briefly. These experimental design conditions were established previous and can be referenced for more detail in the dissertations of on by Santosh Abraham and Kapil Panchal [31, 32]. Conditions of the test section were considered to be unaltered given that all inlet operating conditions, blade profiles and endwalls were kept the same. The upstream purge slot and discrete holes were the only modifications and were done successively for the best possible aerodynamic performance comparisons.

2.5.1 Inlet Flow Measurements

A turbulence grid was placed 5.5 C_{ax} upstream of the cascade, shown in Figure 2.2, in order to obtain the desired level of turbulence intensity of 8%. A single line hot-wire probe was employed to measure the inlet free stream turbulence intensity based on the isotropic turbulence assumption. The incoming flow uniformity was confirmed through aerodynamic measurements

were made on a plane 0.45 C_{ax} upstream of the airfoil leading edge. The upstream flow was measured with pitchwise traverse measurements of a pitot probe and the flow uniformity was established with a maximum deviation of ±0.4% in normalized pressure.

2.5.2 **Static Pressure Measurements**

Airfoil surface static pressure measurements were carried out previously by Abraham and Panchal [31, 32]. The passage flow periodicity was established utilizing the airfoil surface pressure taps. The blade loading was measured, while adjustments to the headboard and tailboard were made until periodic conditions were ascertained. It is clearly seen in Figure 2.10, that the ideal conditions for were met when the headboard was place at 1.16^0 and the tailboard at 48^0 degrees from the horizontal with a cascade angle 30^0, Figure 2.11. show that Abraham [31], was able to achieve good agreement between the experimentally measured blade loading measurements to the CFD derived solution.

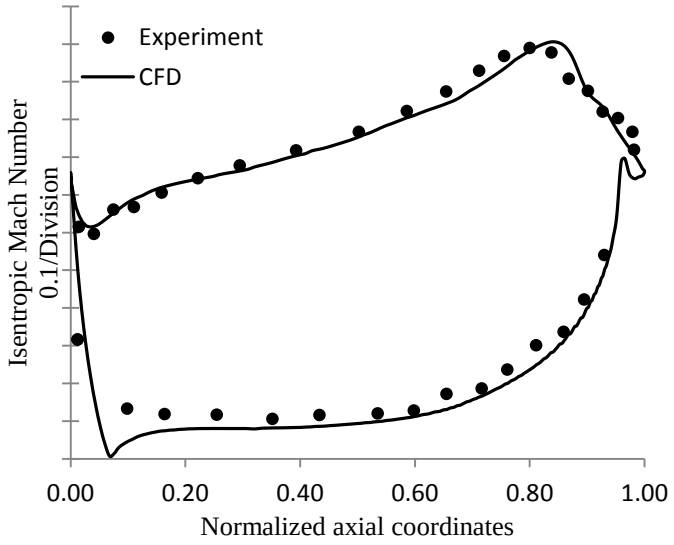

Figure 2.10: Midspan airfoil loading from CFD and experiments (design Mach #) [31]

In order to estimate the inlet/exit Mach numbers and incoming flow uniformity, static pressure taps were positioned on the endwalls of the cascade on a plane 0.5 C_{ax} upstream of the airfoil leading edges and 0.5 C_{ax} downstream of the airfoil trailing edges. Endwall static pressure distribution was already measured during previous year's project and was not performed again. Although, inlet and exit Mach number were calculated for all tests to ensure measurements were carried out at design exit Mach number ~0.88.

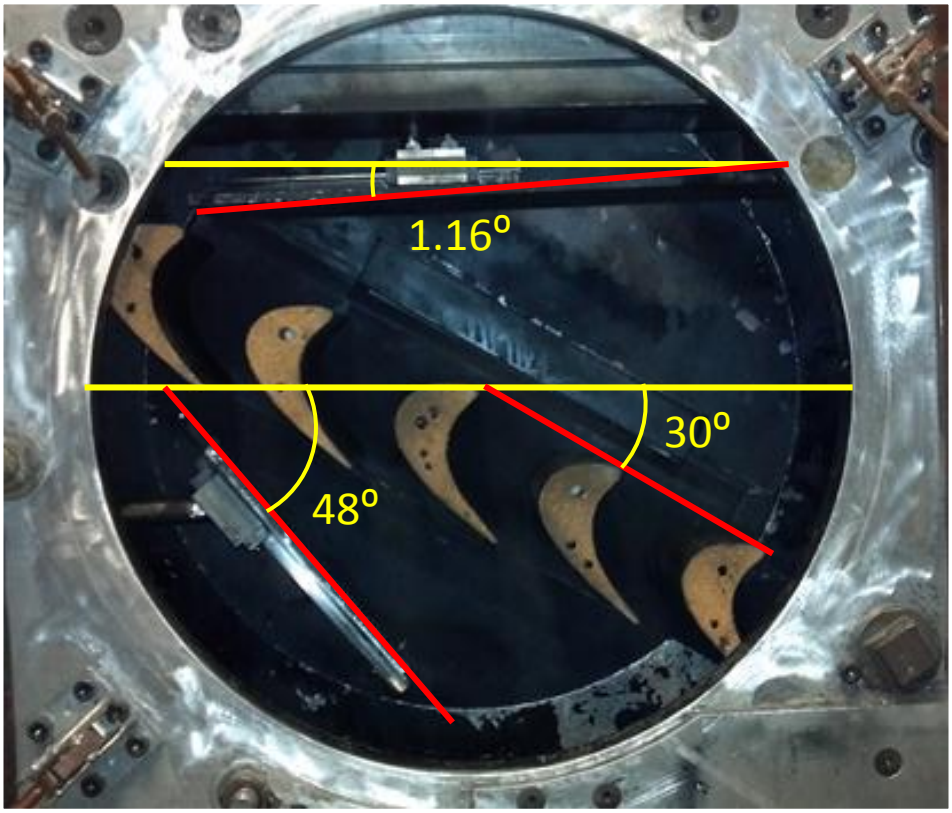

Figure 2.11: Cascade Angles

2.5.3 **Loss Coefficient Measurements**

Performance of two different endwalls (one non-contoured baseline endwall and the other AO contoured endwall) at transonic flow conditions with a design incidence angle and exit Mach number were investigated. For all without and with cooling (coolant MFR 1.0% for upstream slot

and 0.25% for discrete holes) cases, the loss coefficient measurements were carried out at 0.1 axial chord downstream from the blade trailing edge. The mass flow per passage has been estimated to be approximately 1.62kg/s. A pitot probe was used to measure the inlet total pressure at midspan with a closely mounted Kiel probe, located at the upstream slot or the measurement windows in Figure 2.12, in order to verify the measurement accuracy.

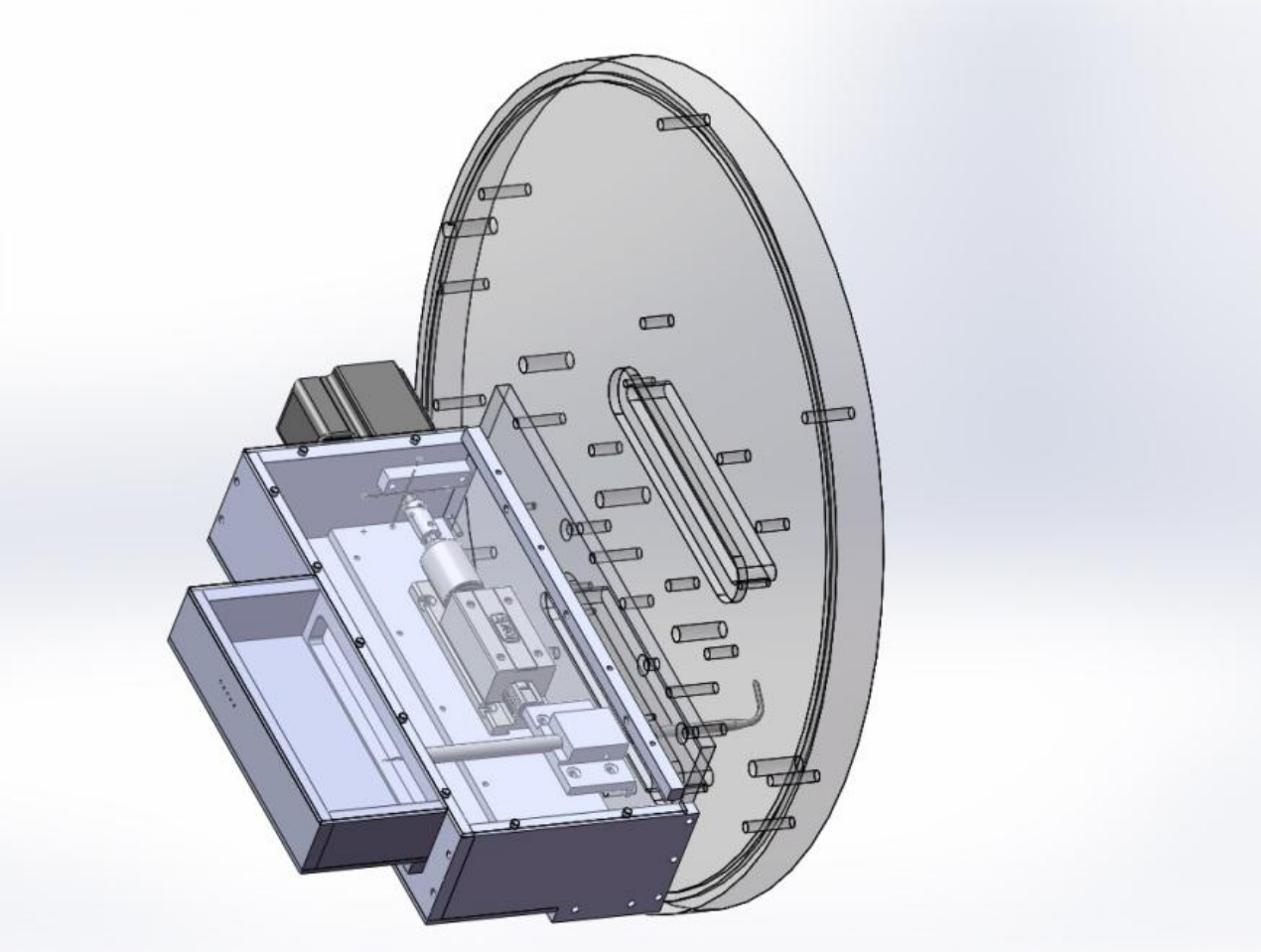

Figure 2.12: Pressure Measurement Window

The spanwise area averaged loss coefficient was calculated using pitchwise total pressure measurements traverse results carried out at eleven different spanwise locations starting from the angled endwall to mid-span at the design exit Mach number by means of a 5-hole probe. Figure

2.13 demonstrates the location and motion of the measurements for the passage of interest. The traverse moved six inches is the spanwise direction with the probe tip oriented along the blade turning angle. This procedure was repeated for measurements up to the midspan location with a distance of 3 inches.

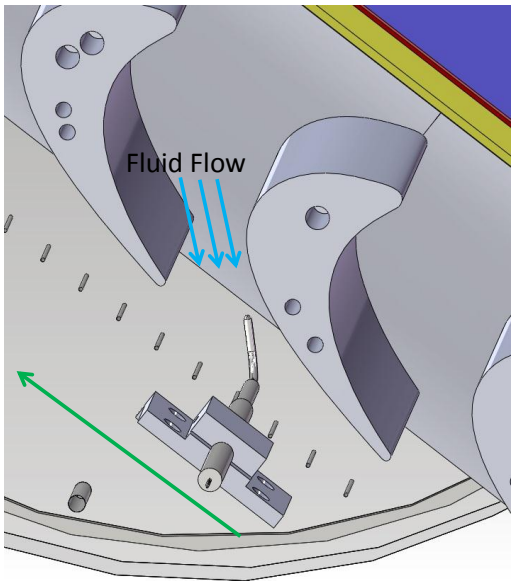

Figure 2.13: Pitchwise and Spanwise Traverse Measurement Location

2.5.4 **Data Acquisition Set Up**

The experimental set up originally utilized four separate computers, an infrared camera, a National Instruments data acquisition system, and a Netscanner 98RK. Due to the complexity of the experiment efforts were made to optimize the experimental set up. A new Labview code was developed that integrated the existing VI, that was responsible for controlling and operating the valve, with the required data acquisition VI for the Siemens experimental set up. The code structure for the tunnel control was copied over into the same work space as the Siemens data acquisition. Throughout testing improvements were made. The integration of the traverse controls were performed as well as a while loop that would automatically signal the traverse to move after a set time delay to accommodate the tunnel response time. Within that same loop two

solenoid valves were controlled. These valves were necessary for the film cooling experiments. The one valve would be open to the atmosphere until the desired temperatures were met. Once the experiment was ready, just as with the traverse the solenoid valves would switch with respect to the time delay so that that coolant would no longer eject into the atmosphere and into the coolant plenum chamber for film cooling. This timing and switch was set up so that the mainstream and coolant flow would meet almost simultaneously in the test section.

The further improvement of the experiment came with the addition of the SendKey.vi within the Siemens Labview program. What this did is once the record command was send in the Labview program, within a second the key strokes, through the use of an AuntoHotKey script, to start the recording of the Netscanner 98RK NUSS software and the FLIR infrared camera software was executed. During this moment in time the operator was able to turn the safety key and execute the "Run Tunnel Button." The last addition to the Labview was the integration of the 8400 PSI pressure scanner. Similar to the traverse control, the code had been previously developed. It was modified and integrated into the Siemens Labview program creating an addition 32 pressure channels for measurement. Along with the Netscanner's 48 available channels this modification now provides the possibility of 80 pressure measurement channels. The Labview program structures and AutoHotKey script are described in more detail in Appendices II and III, respectively.

This new Labview program in conjunction with the AutoHotKey script allowed for all the programs to be operated and controlled from a single computer. The programs improved timing between time of execution, increased accuracy and repeatability in time of measurement with respect to the wind tunnel blow down, and in the data acquisition. The data was able to be consolidated into less files, the timing aided in removing unnecessary dead time data, and data

synching. The current set up is now able to allow the experiments to be performed by one controller.

2.5.5 **Post Processing for Aerodynamic Experiments**

After the data is collected from an experiment, the data recorded by the 5-Hole probe and the upstream pitot probe needs to be extracted for the time it is being traversed. The key component is to know when the probe is moving relative to the tunnel start time. This was done by creating a conjugate system. The pressure system used the Netscanner 95-RK coupled with the National Instruments Data Acquisition instrumentation. The pressure scanner measured all the pressures of interest where the NI-DAQ system measured the mainstream air temperatures conditions for the heat transfer experiments. In order to couple the two independent systems a pitot probe upstream of the test section was used. The total pressure line was branched off using a "T" configuration. One pressure line went directly to the Netscanner and the other line went to a pressure transducer. The pressure transduced than created a voltage that was read by the NI-DAQ system. Due to the use of multiple instruments the record times needed to be synched, a clear time lag between the two pressure profiles cab be seen in Figure 2.14.

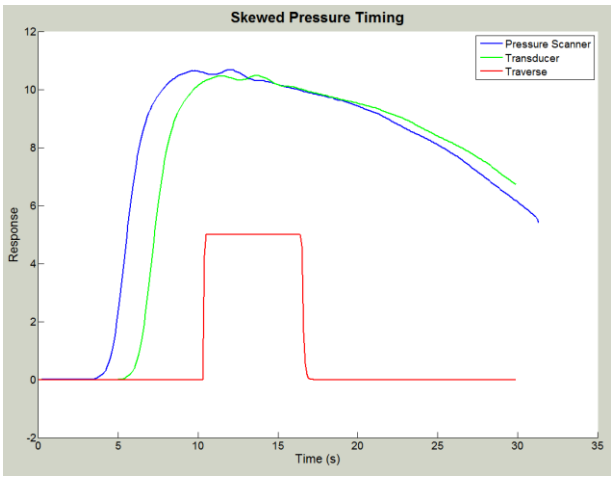

Figure 2.14: Time lag between Netscanner 98RK and NI_DAQ pressure measurements.

The mainstream pressure profile created by the tunnel could then match between the two independent systems by using a simple MATLAB code, which can be found in Appendix I for more information. Figure 2.15 shows an example of an time shift synching the appropriate data between the separate data acquisition systems.

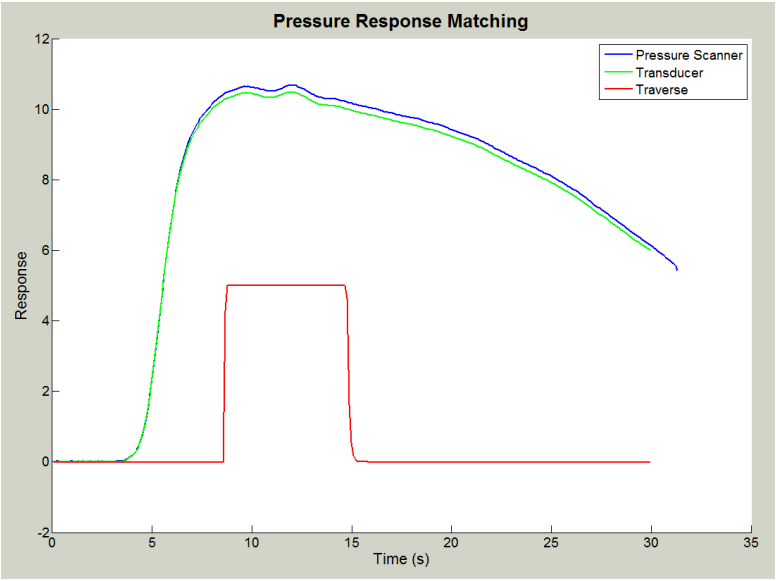

Figure 2.15: Tunnel pressure profile time data shift

The importance is that that when the traverse is moving it sends a voltage to the NI-DAQ. During the time the traverse is moving, the voltage output is represented through what looks like

a square wave. Now that the wind tunnel blow down pressure profile and traverse motion has been recorded. The time of motion, a total of 6 inches at 1in/sec, is known relative to the pressure profile. Using this time interval the corresponding pressures for the 5-hole probe and upstream pitot probe can be extracted from the pressure scanner data as seen in Figure 2.16.

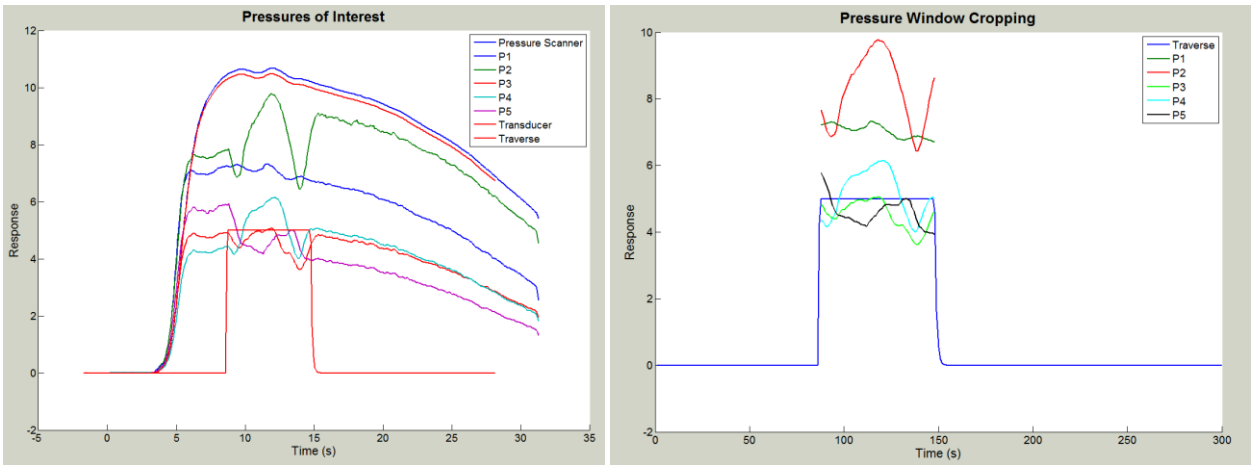

(a) (b)

Figure 2.16: Tunnel profile and 5 hole probe pressures measured by the NI-DAQ and Netscanner (a) Pressure profiles for entire experiment run time (b) Five hole probe pressure cropping.

The 5-hole pressure data is then processed using the calibration data for the probe. The calibration data and probe were purchased from Aeroprobe. The calibration data is loaded into a MATLAB code along with the five pressures and outputs the total and static pressures and flow angles in the spanwise and pitchwise directions. The code was developed previously at Virginia Tech utilizing similar methodologies found from the works of Ligrani et al. Main et al., and Pisasale and Ahmed [33-35]. Utilizing the equations below the code uses a hyper-surface fitting for the multidimensional Mach number calibration data base in order to interpolate between coefficients developed from the calibration data and the experimental data.

$$\bar{P} = \frac{P_2 + P_3 + P_4 + P_5}{4} \qquad \textbf{Equation 2.2}$$

$$Cp_{yaw} = \frac{(P_2 - P_3)}{(P_1 - \bar{P})} \qquad \textbf{Equation 2.3}$$

$$Cp_{pitch} = \frac{(P_4 - P_5)}{(P_1 - \bar{P})} \qquad \textbf{Equation 2.4}$$

$$Cp_{Ma} = \frac{(P_1 - \bar{P})}{(P_1)} \qquad \textbf{Equation 2.5}$$

Now that the local total pressure at the exit of the test section are known. The loss coefficient at 0.1 C_{ax} can be calculated. The pressure scanner measured the total inlet pressure upstream of the test section. The appropriate pressure values for the upstream total pressure and the 5-hole probe derived total and static pressures are then evaluated at their respective times. The following equation was then used to calculate the loss coefficient, where omega (ω) symbolically represents the loss coefficient.

$$\omega = \frac{Pt_{in} - Pt_{ex}}{Pt_{ex} - Ps_{ex}} \qquad \textbf{Equation 2.6}$$

2.5.6 **Uncertainty in Loss Coefficient Measurements**

The equation of loss coefficient is:

$$\omega = \frac{p_{t\_in} - p_{t\_ex}}{p_{t\_ex} - p_{s\_ex}} \qquad (1)$$

Using Kline and McClintock's [36] method

$$w_\omega = \left[\left(\frac{\partial \omega}{\partial p_{t\_in}} w_{pt\_in}\right)^2 + \left(\frac{\partial \omega}{\partial p_{t\_ex}} w_{pt\_ex}\right)^2 + \left(\frac{\partial \omega}{\partial p_{s\_ex}} w_{ps\_ex}\right)^2\right]^{\frac{1}{2}} \qquad \textbf{Equation 2.7}$$

$$w_\omega = \left[\left(\frac{\partial\omega}{\partial p_{t\_in}} w_{pt\_in}\right)^2 + \left(\frac{\partial\omega}{\partial p_{t\_ex}} w_{pt\_ex}\right)^2 + \left(\frac{\partial\omega}{\partial p_{s\_ex}} w_{ps\_ex}\right)^2\right]^{\frac{1}{2}} \qquad (2)$$

Where, w = uncertainty

$$\frac{\partial\omega}{\partial p_{t\_in}} = \frac{1}{(p_{t\_ex} - p_{s\_ex})} \qquad (3)$$

$$\frac{\partial\omega}{\partial p_{t\_ex}} = -\frac{(1+\omega)}{(p_{t\_ex} - p_{s\_ex})} \qquad (4)$$

$$\frac{\partial\omega}{\partial p_{s\_ex}} = \frac{\omega}{(p_{t\_ex} - p_{s\_ex})} \qquad (5)$$

Combining equation [2-5] yields,

$$w_\omega = \left[\left(\frac{1}{(p_{t\_ex} - p_{s\_ex})} w_{pt\_in}\right)^2 + \left(-\frac{(1+\omega)}{(p_{t\_ex} - p_{s\_ex})} w_{pt\_ex}\right)^2 + \left(\frac{\omega}{(p_{t\_ex} - p_{s\_ex})} w_{ps\_ex}\right)^2\right]^{\frac{1}{2}}$$

$$\Rightarrow \frac{w_\omega}{\omega} = \frac{1}{(p_{t\_ex} - p_{s\_ex})}\left[\left(\left(1 + \frac{1}{\omega}\right) w_{pt\_ex}\right)^2 + \left(\frac{w_{pt_{in}}}{\omega}\right)^2 + \left(w_{ps\_ex}\right)^2\right]^{\frac{1}{2}} \qquad (6)$$

The isentropic Mach number definition is defined on p_{t_in} and p_{s_ex}. Assuming the process is isentropic, it can be stated that $p_{t\_ex} = p_{t\_in}$. After substituting, $\frac{p_{t\_in}}{p_{s\_ex}} = \left(1 + \frac{\gamma-1}{2} M_{iso}^2\right)^{\frac{\gamma}{\gamma-1}}$ into equation (6) gives

$$\frac{w_\omega}{\omega} = \frac{1}{p_{s\_ex}\left[\left(1+\frac{\gamma-1}{2}M_{iso}^2\right)^{\frac{\gamma}{\gamma-1}} - 1\right]}\left[\left(\left(1 + \frac{1}{\omega}\right) w_{pt\_ex}\right)^2 + \left(\frac{w_{pt_{in}}}{\omega}\right)^2 + \left(w_{ps\_ex}\right)^2\right]^{\frac{1}{2}} \qquad (7)$$

Now for a given Mach number and related p_{s_ex}, we can calculate uncertainty in experimental results for a given value of loss coefficient, if the uncertainties in individual variables are known.

Uncertainty in p_{t_in}: The total pressure (p_{t_in}) is measured using 9816-2675 module with a 20 psi range. Instrument accuracy is 0.05% FS, which is $\pm 0.01\ psi$. Also, we use mean of the acquired data points along the run when inlet total pressure remains fairly constant. Two experimental runs with identical settings on two different days shows about 0.05 psi difference. Thus, the uncertainty (Instrument accuracy + uncertainty due to unsteadiness of total pressure) can be given as,

$w_{pt\_in} = \pm 0.06\ psi$ (8)

Uncertainty in p_{t_ex}: The instrument accuracy remains same. Now, even at 1 axial chord downstream, the flow is not completely mixed out and hence when we average the total pressure Again, the uncertainty is based on the repeatability of the mean value of p_{t_ex}. A conservative value of ± 0.07 is estimated. Giving,

$w_{pt\_ex} = \pm 0.09\ psi$ (9)

Uncertainty in p_{s_ex}: p_{s_ex} is the wall static pressure measured 0.5 axial chord downstream. The values are generally below 2.5 psi and the instrument accuracy is 0.15 %FS, i.e. $\pm 0.03\ psi$. The variation in static pressure is about $\pm 0.38\ psi$. As previously,

$w_{ps\_ex} = \pm 0.10\ psi$ (10)

Hence, uncertainty in all the variables is of same order, say w_{exp}.The equation (7) becomes,

(11) $$\frac{w_\omega}{\omega} = \frac{W_{exp}}{p_{s\_ex}\left[\left(1+\frac{\gamma-1}{2}M_{iso}^2\right)^{\frac{\gamma}{\gamma-1}}-1\right]}\left[\left(1+\frac{1}{\omega}\right)^2+\left(\frac{1}{\omega}\right)^2+1\right]^{\frac{1}{2}}$$ **Equation 2.8**

Now, for 60^o inlet angle the loss coefficient range is about 0.03 to 1.9.

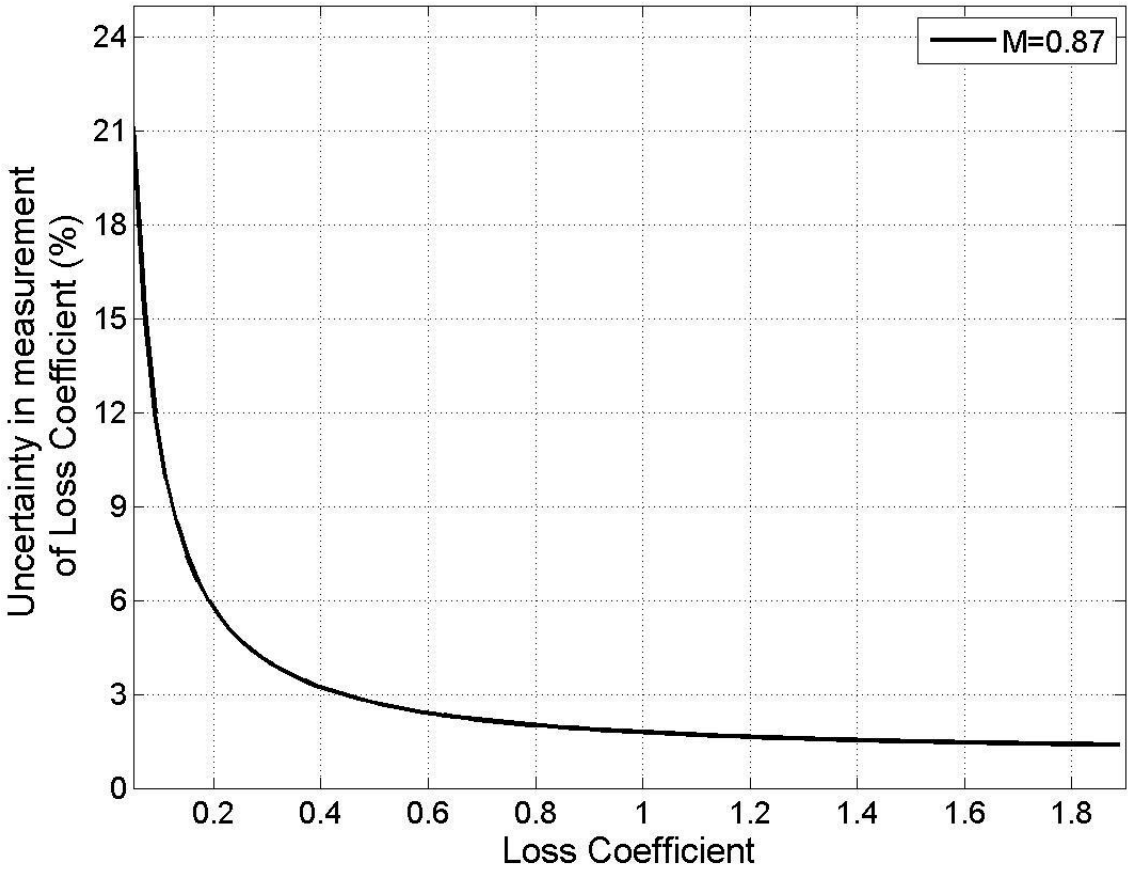

Figure 2.17: Variation in uncertainty with loss coefficient and Mach number

A value of $\boldsymbol{w_{exp} = \pm 0.07\ psi}$ was taken as a reasonable estimate from the work of Santosh Abraham [31] and was used in producing Figure 2.17. It can be observed that percent uncertainty is inversely proportional to the loss coefficient value. At an uncertainty of 20% $\omega = 0.03$ giving a $\Delta\omega = \pm 0.006$, and and at about 2% uncertainty at $\omega = 1.9$ results in $\Delta\omega = \pm 0.038$

$$\boldsymbol{\omega_{actual} = \omega_{measured} \pm 0.038} \qquad (12)$$

Utilizing the equation above, the actual loss coefficient can be found on Figure 2.17 and the corresponding uncertainty can pulled from the graph.

Chapter 3: Aerodynamic Experiments –Upstream Slot Cooling

3.1 Overview

The aerodynamic performances of two different enwall designs were studied in the presence of an upstream leakage slot. The first endwall geometry, referred to as the Baseline endwall, is a non-contoured endwall. The second endwall geometry is a contoured geometry that was obtained from an optimization study to minimize the aerodynamic losses, which yielded its name the Aero Optimized or AO endwall. The upstream purge slot utilized in both endwall geometries had the design, dimensions, and location held constant.

The aerodynamic experiments consisted of eleven tests to capture a view of the flow at $0.1C_{ax}$ chord downstream of the trailing edge of the blades. A set of repeatability experiments of eight tests, were performed to ensure consistency in the results and a detailed explanation of the experimental methodology used in this procedure is mentioned previously in section 2.5 of this report. Measurements of the flow were conducted for both cases of no blowing and with blowing to further understand the influences brought on by the backward facing step present with the slot and the with the addition of coolant.

3.2 Effect of Slot (No Blowing)

The addition of slot $0.29\ C_{ax}$ upstream of the leading edge was implemented in order to do film cooling experiments. The heat transfer coefficient and effectiveness were to be examined with the two endwall geometries. However, the effects on the aerodynamic performance with the backward facing step in conjunction with blowing were also of concern.

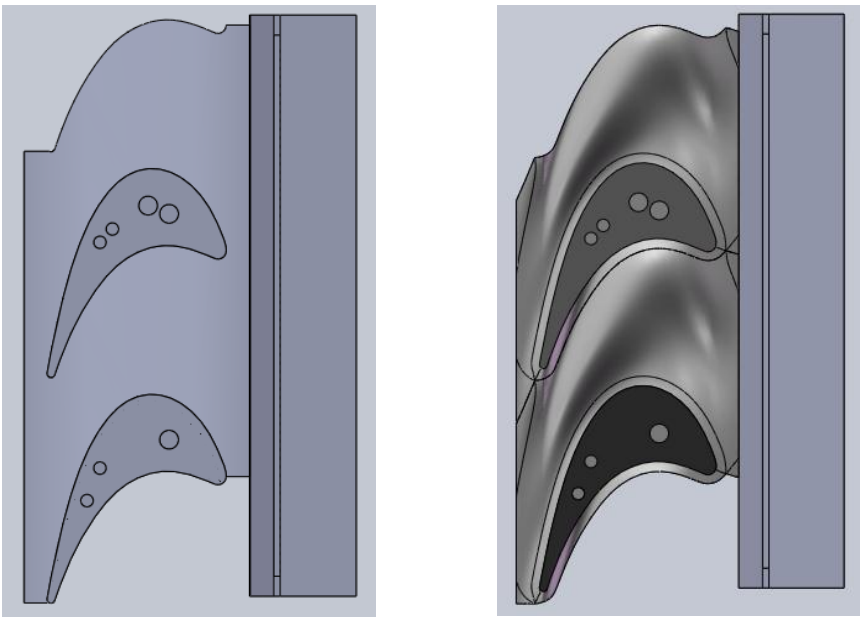

Figure 3.1: (a) Baseline (b) and AO contoured geometries with upstream leakage slot.

There have been some studies on the aerodynamic performance of blade profiles with different types of injection slots. As mentioned before a study performed by Blanco and Hodson [37], yielded similar results. In their case they looked into the effects of a backward and forward facing step with a cavity. They also did cases of no leakage and leakage flow. Their findings were that the backward facing step yielded better performance than the forward facing step. This was primarily due to how the inlet boundary layer is affected.

The presence of the slot affected the location and intensity of the loss cores. The significant changes that arise are that the loss cores migrate further into the midspan with more mixed out losses throughout the span. The losses near the endwall tend to change depending on the geometry. The changes near the endwall may be due to a change in the intensity of the suction side vortex. These trends will be explained further for the two geometries in the next couple of sections.

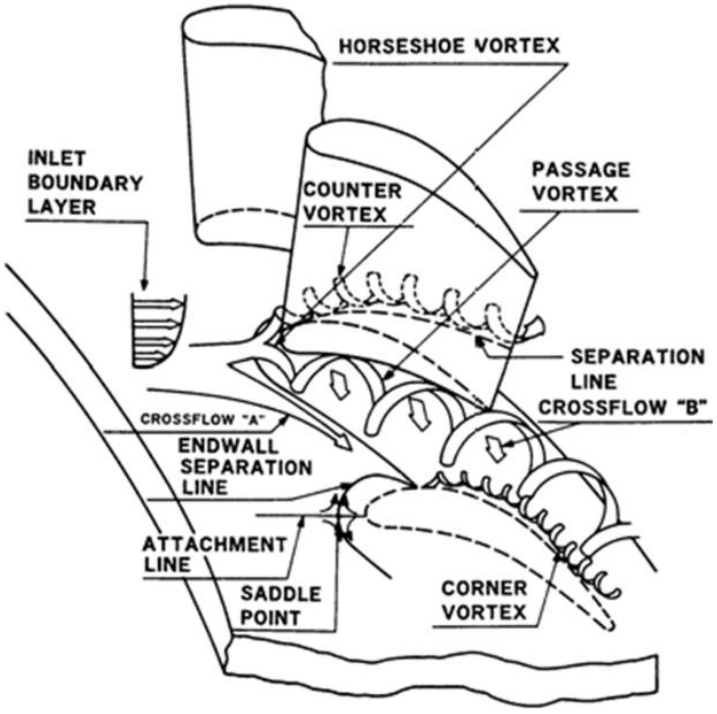

Figure 3.2: Secondary Flow in Turbine Cascades (Takeishi et al. [38])

In the typical passage without a backward facing step the passage flow characteristics can be described with Figure 3.2. For further understanding of the flows that develop within an axial turbine papers by Langston and Lampart [39, 40] have detailed flow models developed from CFD and experimental data. The losses visible near the endwalls are a result of complex vortices due to the secondary flows. The pressure gradient in the passage caused by the boundary layer velocity distribution and flow stagnation on the blade create secondary flows in the end wall region. The pressure variations push the flows towards the endwall and lead to the development of the two legs of the leading edge vortex. The turning angle of the flow between the airfoils creates a strong pressure gradient across the passage. This pressure gradient influences the strength and path of the two legs of the horseshoe vortex and the low velocity flow near the endwall. The pressure side leg is forced to flow in a downward direction and combines with the

low velocity flow near the endwall and forms the passage vortex. The passage vortex drifts from the pressure side leading edge toward the suction side trailing edge of the adjacent airfoil. As the passage vortex nears the suction side, it lifts off the endwall and adheres along the suction side and moves downstream in the passage. At the same time the suction side horseshoe vortex remains close to the endwall until it meets with the passage vortex. At this time it wraps itself around the passage vortex instead of adhering to the suction surface, lifts off the end wall and continues downstream along the suction side.

It was clearly discussed in the literature survey, that the slot flow for low and high speed flows significantly alter the secondary flow development within the passage. The upstream slot can disrupt the incoming boundary layer effect the endwall pressure variations as well as the pressure gradient throughout the passage. Even in some cases, the location of the slot can even diminish the strength or pre-start saddle point development of the horseshoe vortex.

Looking into the experimental data, there was a shift in location and lower intensity of the loss cores further midspan, this gives reason to believe that the slot plays a role in first diminishing the strength of the passage vortex and then causes the passage vortex to lift off of the endwall at an earlier time and combine with the suction side vortex at a later time. In referencing the CFD results contributed by Siemens in Figure 3.3 (a) & (b) it is clear that the strength and direction of the passage vortex is significantly altered. The flat endwall case with no cavity has a perfectly formed passage vortex which developed off the leading edge and at approximately 0.5 C_{ax} downstream from the leading edge, the suction side vortex meets with the passage vortex and continues along the suction side surface. Figure 3.3 (b), distinctly illustrates how the slow disrupts the formation of the passage vortex. The formation of other secondary vortices from the slot is not completely unexpected when referring back to the literature. The slot

alters the cross flow within the passage directing the passage vortex along another trajectory which causes it to meet up with the suction side surface at approximately 0.75 C_{ax} from the leading edge. The diminished strength of the passage vortex was evident in the loss contours and heat transfer results showed a significant reduction endwall heat transfer just with the addition of the slot and no purge flow. Further analysis of the effect of the slot for each geometry will be explored next.

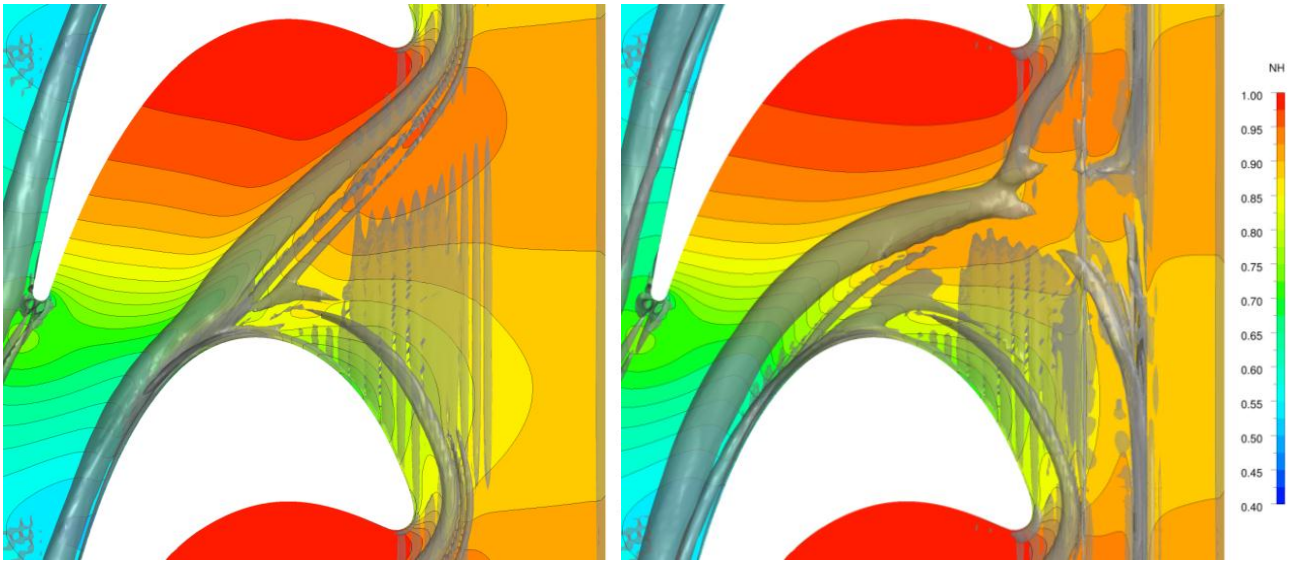

Figure 3.3: (a) Flat Endwall: No Cavity (b) Flat Endwall: With Cavity 0% Purge

3.2.1 **Baseline with Slot vs. without Slot**

The Baseline geometry has a diverging endwall, where the exit span was increased relative to the inlet span resulting in a 13^0 angle. The airfoil span increases by about 16% linearly in the axial direction, aiding to simulate the required leading edge loading in a quasi-2D cascade. The addition of the slot upstream creates a backward facing step with a height of about 0.14in (3.62mm), with a 0.48in (12.3mm) chamfer at an incline angle of about ~17^0. For

reference this is compared to a previously incoming boundary thickness for this test section of about ½ inch (12.7mm).

The upstream slot was placed ~0.29 C_{ax} upstream from the leading edge. Though the physical differences do not seem significant the changes that have occurred with the addition of the upstream slot are more clearly seen when the losses for the same geometry without the presence of a slot and cavity are compared. In the presence of the slot the loss core associated with the passage vortex has moved closer to the midspan and has decreased in intensity (See Figure 3.4 (b)). This is due to the interaction between the inlet boundary layer and the flow inside the cavity. The vortex for the no slot case can be identified by the region of high losses at a span of ~2-3 inches and for the slot case at ~2.5-3 inches.

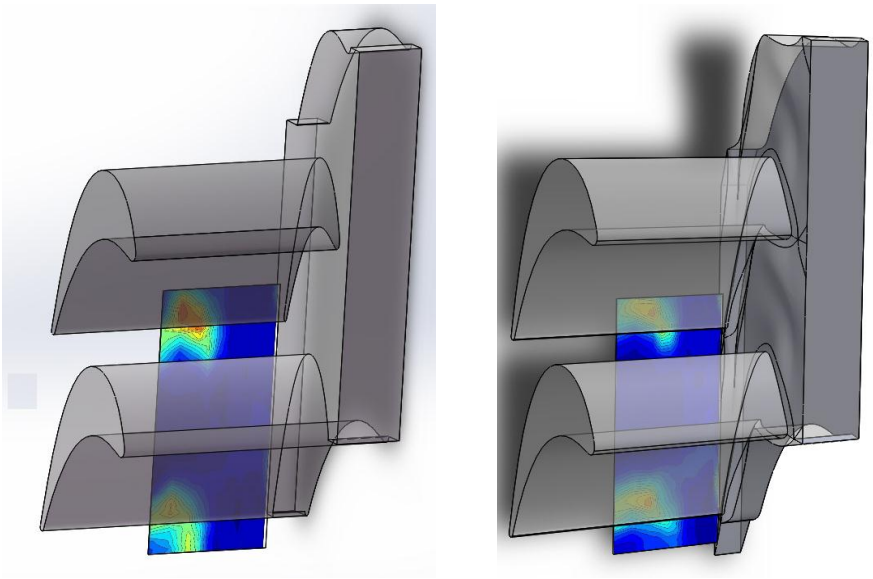

Figure 3.4: (a) Baseline & (b) Aero Contoured without an Upstream Slot

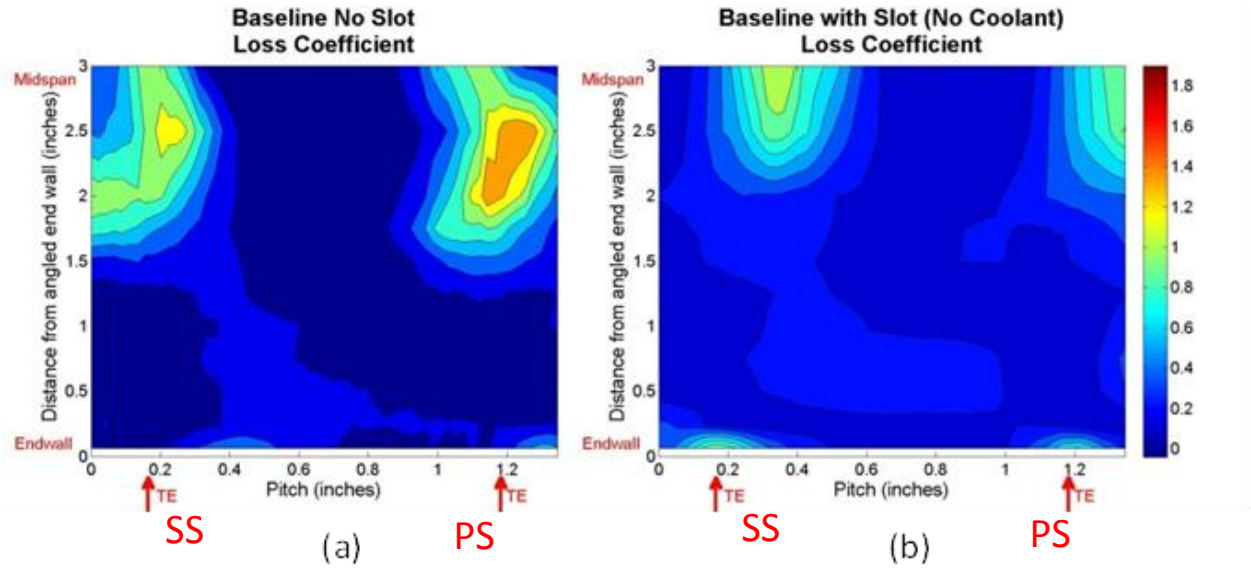

Figure 3.5: Baseline Geometry Loss Coefficient at 0.1 C_{ax} downstream of the trailing edge (a) without Leakage Slot vs. (b) With Leakage Slot

In the case of no leakage flow, part of the mainstream fluid is swept into the cavity. This directly results in a reduction in strength of the pressure side leg of the horseshoe vortex. It is noticeable that the slot case seems to have higher endwall flows. This could be due the cavity leaking fluid into the low pressure part of the mainstream and with the decreased strength of the passage vortex allowing the suction side corner vortices to grow in size and intensity. Lastly, it is seen that there is an increase in the net mixed-out endwall losses relative to the case with no cavity. This is believed to be due to the inlet boundary layer separating due to the backward facing step. As a consequence the flow is unable to reattach before it meets the leading edge causing a thickening of the inlet endwall boundary layer thereby increasing the secondary losses. Despite, the drastic change in secondary flow structure, the losses produced by the slot compared to the benefits of the reduction in passage vortex intensity balance out. Overall without the addition there is approximately 0% difference area averaged losses when comparing the slot and the no slot cases.

3.2.2 **AO with Slot vs. without Slot**

The AO contoured geometry has a protruded region which starts near the true leading edge of the airfoil and proceeds towards the suction side of the adjacent airfoil. Normally this protrusion prevents the passage vortex or the pressure side leg of the horseshoe vortex from cutting sharply across the passage, from leading edge pressure side to suction side. The passage vortex tends to move across the passage due to the existing large pressure gradient. But the peaks on the contoured endwall try to guide this passage vortex along the pressure side of the airfoil, thereby delaying the progression of the passage vortex in the cross passage (pitchwise) direction. It was observed and presented in Abraham's dissertation [31] that the passage vortex is guided along the favorable streamwise direction by the contours. The contours succeed in making the passage vortex meet the suction side leg of the horseshoe vortex further downstream, than in the baseline case. As the cross flow direction of the passage vortex, compared to the streamwise mainstream flow, is less intense in the aero-optimized contoured endwall case, the secondary losses generated will be lower.

This passage vortex is identified in Figure 3.6 (a) at a normalized span of 1.25 to 2.5 inches for the no slot AO contoured case. The contours succeeded in restricting the amount of lift-off of the passage vortex for the no slot case. This is due to the fact that the passage vortex was delayed in meeting the suction side leg of the horseshoe vortex, which is where the lift off originates. However, the flow structures and locations have changed due to the presence of the slot. The mixed out losses that were seen in the Baseline case is not as prevalent in the Aero contoured case. From the results presented in the dissertation of Santosh Abraham [31], the contouring of the endwall was able to smoothen out the pressure variations from the pressure side of the airfoil to the suction side of the adjacent airfoil. This alters the passage vortex flow

path favorably by reducing the adverse pressure gradient that is seen in the Baseline geometry. The contouring could thus be reducing the losses produced by the secondary flows. Unlike the Baseline case, where endwall flows increased with the presence of a slot there seems to be a slight reduction in the AO contoured. The addition of the upstream purge slot increases loss production by about 14%.

Between the two slotted geometries, the AO contoured geometry performed worse than the Baseline by 5% in area averaged losses. This is a significant considering the data presented in Santosh Abraham' dissertation [31] shows that the Aero contoured geometry reduces the losses enough to have an 8% increased performance over the baseline geometry without an upstream slot.

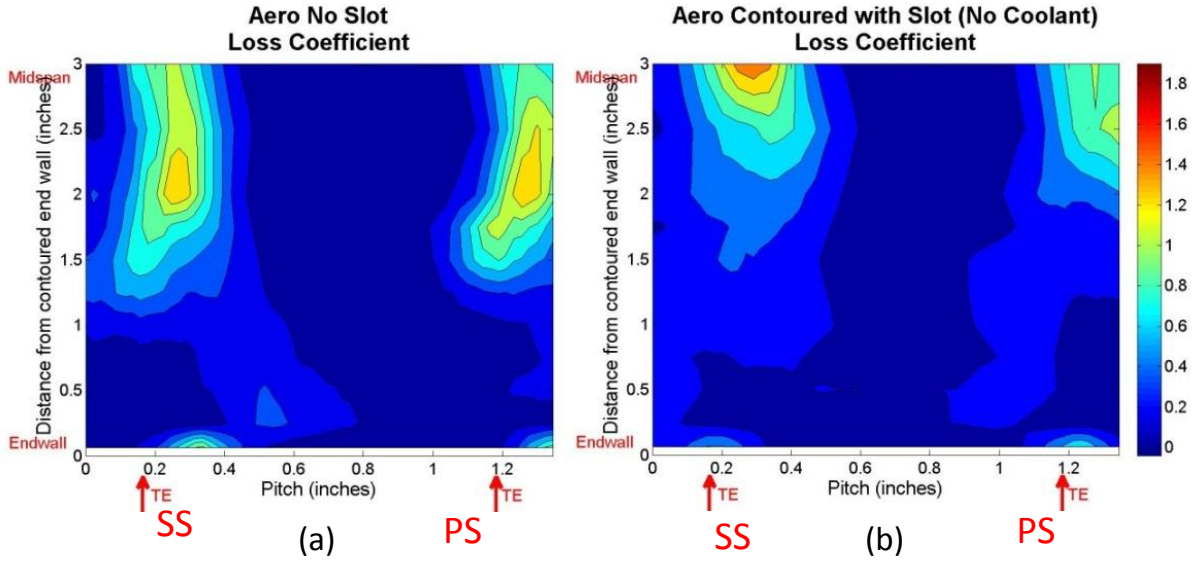

Figure 3.6: AO Geometry Loss Coefficient at 0.1 C_{ax} downstream of the trailing edge (a) without Leakage Slot vs. (b) With Leakage Slot

The Baseline case loss core focal point has moved closer to the midspan due to the inlet boundary layer separation from the backward facing step. A similar shift is seen by observing the passage vortex in the loss counter seen in Figure 3.6 (b). This could be an indication that the contouring is unable to keep the passage vortex attached and redirected on the endwall surface as

it performed with the no upstream slot case. With a combined look into the loss contours with the CFD results performed by Siemens, the passage flow structures have significantly changed. (See Figure 3.7 (a) & (b)) It looks to be that the presence of the slot disrupts the flow in such a way that it decreases the intensity of the pressure side leg vortex so much that when it encounters the contoured regions, the vortex is unable to sustain itself and diffuses. An unforeseen development was a vortical structure that developed due to the slot. The vortical structure originates at the cavity almost at half pitch. This main vortical structure will be referred to as the cavity vortex and can be considered as repositioned passage vortex. The cavity vortex propagates through the passage along the mainstream flow path and connects with the suction side leg vortex at a position slightly further downstream than was seen with the AO contoured geometry with no cavity.

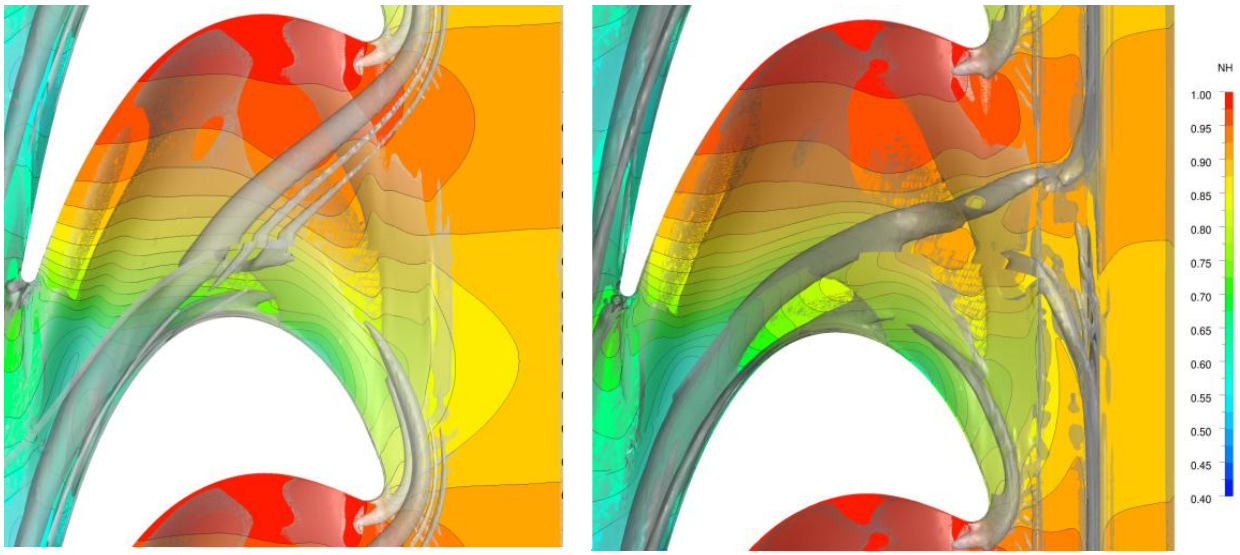

Figure 3.7: (a) AO Contoured: No Cavity (b) AO Contoured: With Cavity 0% Purge

3.2.3 **Effect of Endwall Contouring and Film Cooling**

The focus of this section is to continue the investigation of the aerodynamics of the two geometries, Baseline and Aero contoured. Previously discussed, was how the two geometries performed with the added upstream leakage slot. The AO contoured performed worse in the presence of a slot. The discussion ahead will entail how the two compare with the addition of blowing at 1% MFR of the mainstream.

3.2.4 **Effect of Coolant Injection (Baseline & AO)**

The aerodynamic performances of the geometries were performed only for one blowing ratio of 1% MFR. In comparison to the non-blowing cases of the leakage slot, the area averaged losses increase for the blowing cases, Figure 3.8 (a) & (b) and Figure 3.9 (a) & (b). With 1.0% MFR blowing, the Baseline and AO contoured geometry's area average losses increase by approximately 4% and 3%, respectively. The overall magnitudes and shapes are relatively unchanged. There are slightly more mixed out losses throughout the span. It is difficult to discern if with 1% blowing the loss cores have migrated slightly closer to the midspan or if the vortices have decreased in size and magnitude. Despite this change, it is clear that the upstream leakage slot is responsible for increased losses and an altered secondary flow development compared to the cases with no cavities.

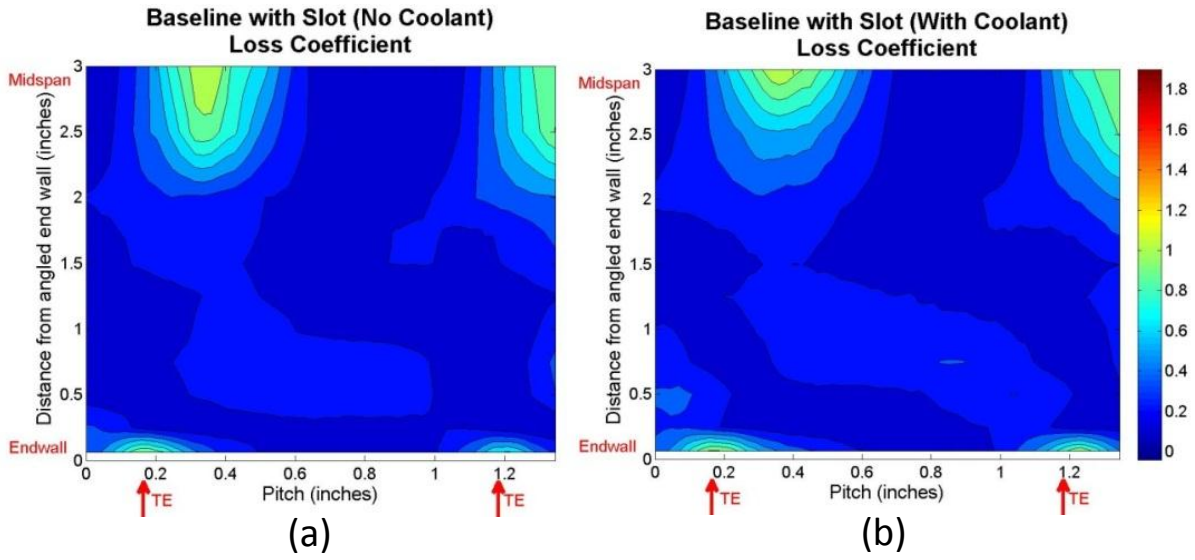

Figure 3.8: Baseline with upstream slot Loss Coefficient at 0.1 C_{ax} downstream of the trailing edge (a) 0% vs. (b) 1% purge.

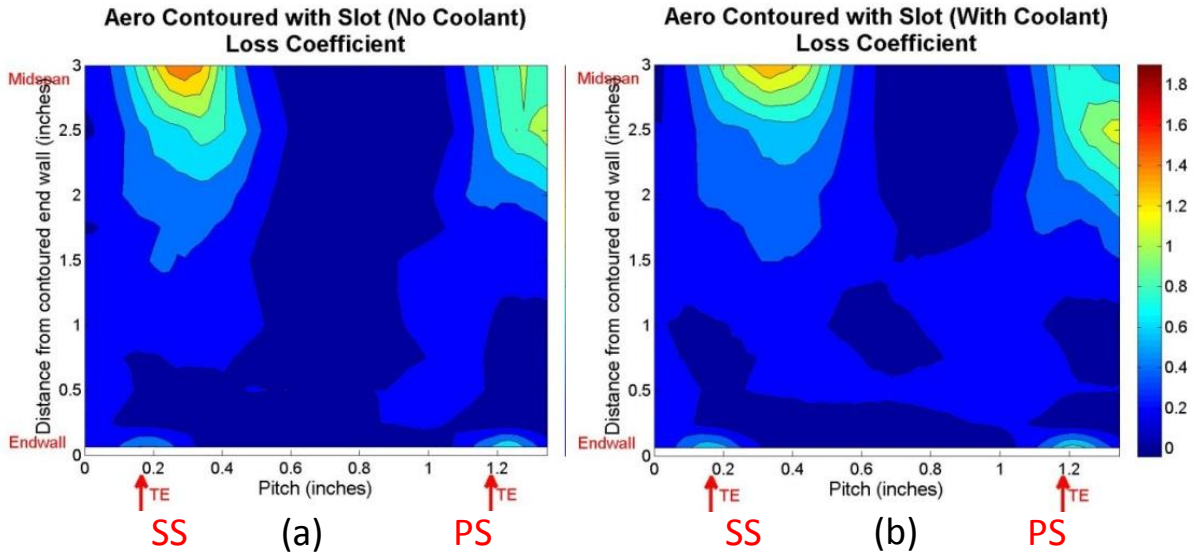

Figure 3.9: Aero with upstream slot Loss Coefficient at 0.1 C_{ax} downstream of the trailing edge (a) 0% vs. (b) 1% purge.

3.2.5 **Effect of Endwall Contouring (Baseline vs. AO - without Coolant)**

The spanwise plot presented below in Figure 3.11, demonstrates the same information presented in the contour plots previously mentioned. This is just another visual aid to help understand how the losses are distributed throughout measurement plane at 0.1 C_{ax} downstream of the trailing edge. The spanwise plots were created by using a line averaging method for the loss coefficient values in the pitchwise direction, which is a total of sixty-one data points. Each average was taken with reference to the trailing edge location of each blade. In order to try to capture higher resolution on the near endwall flows, data points where taken at every quarter inch throughout the span up until the last three points which were incremented at a half inch intervals. There were a total of eleven spanwise measurement locations for a maximum span measurement of three inches.

Starting at the endwall, in the spanwise plot the Baseline geometry has higher endwall loses produced by the suction side corner vortices. At 0.05-0.3 normalized span, the Baseline and Aero contoured losses decrease and increase throughout this area. The amount that each one reduces in their losses in the section is offset by how much they increase. For the remainder of the spanwise loss trend they follow closely with increased losses. At the midspan the AO contoured geometry contains higher losses around the region of the passage vortex. The AO contoured has an overall 5% reduction in losses compared to the Baseline.

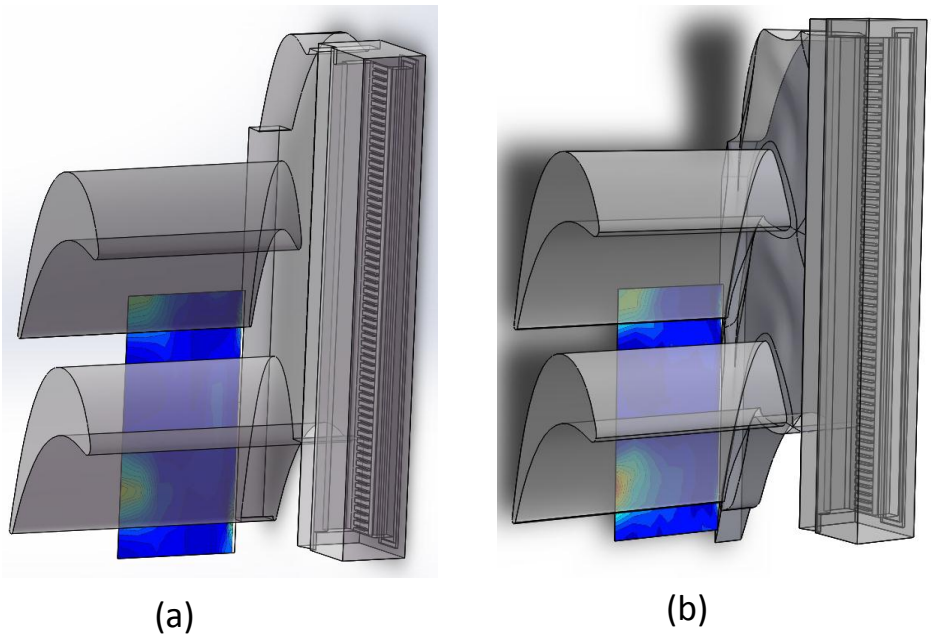

Figure 3.10: (a) Baseline & (b) Aero Contoured with slot 0% Purge Flow

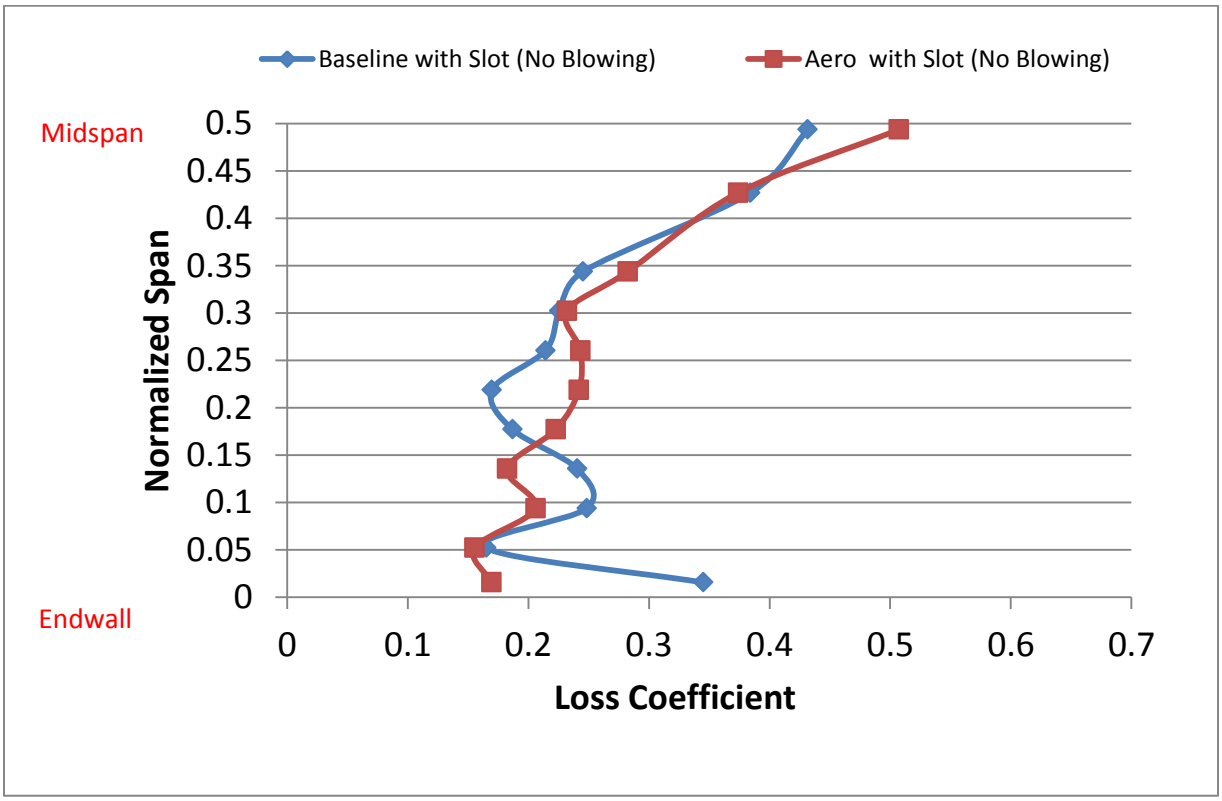

Figure 3.11: Spanwise variation of Loss Coefficient: 0.1 C_{ax} downstream (Baseline vs. AO - without coolant)

3.2.6 **Effect of Endwall Contouring (Baseline vs. AO - with Coolant)**

The losses near AO contoured endwall, for the 1% percent blowing case is unaffected. However, there is a slight increase in the corner vortices for the Baseline geometry. As with the no blowing case the trends throughout the span are very similar, though their troughs and peaks occur at locations slightly further into the midspan with increased magnitudes. Despite the fact that the Baseline geometry has lower loses than the AO contoured geometry from about 0.25-0.4 normalized span. The reason for the shift in troughs and peaks is due to the coolant blowing pushing the already separated flow further out. The coolant is increasing the endwall boundary layer allowing for higher intensity secondary flow development. The AO contoured geometry seems to control near endwall flows better than the baseline geometry. With 1% purge flow, the AO contoured geometry again has higher losses than the baseline, yielding an overall 4% increase in losses. The spanwise trends certainly point out that the coolant injection induce higher losses by energizing the secondary flows and that the slot diminishes the added benefits of the AO contoured geometry seen for the case without a slot. This brings to mind that a new optimization study may necessary to be conducted with an upstream slot geometry taken into consideration.

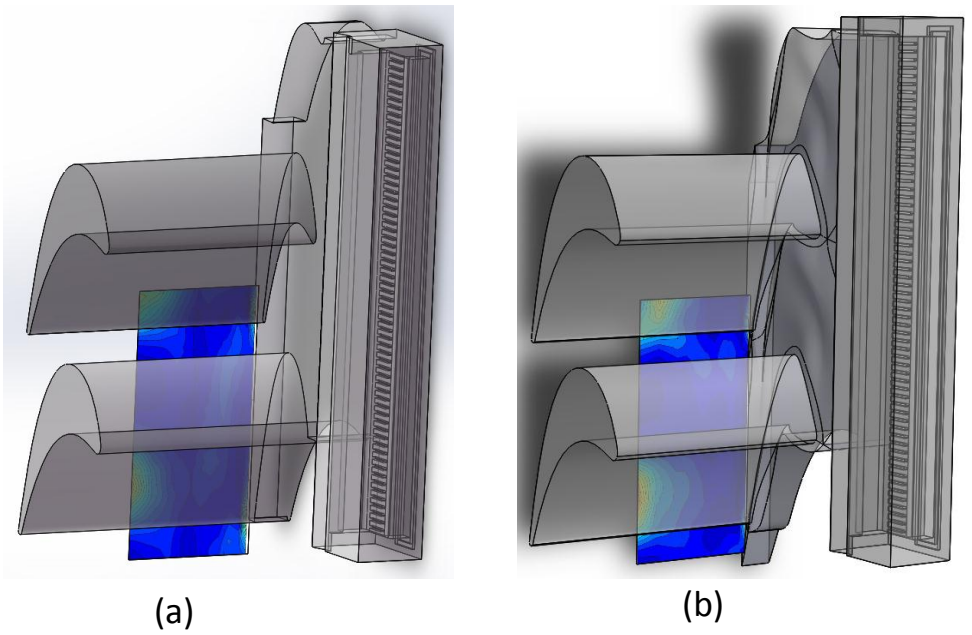

Figure 3.12: (a) Baseline & (b) Aero Contoured with slot 1% Purge Flow

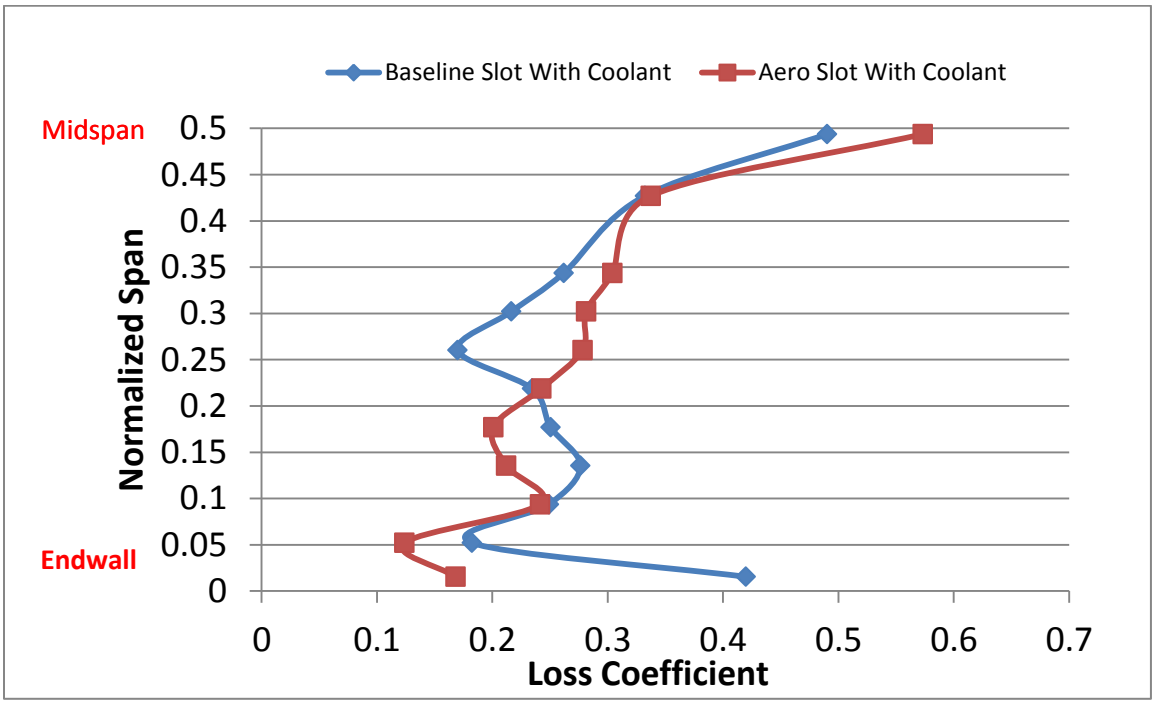

Figure 3.13: Spanwise variation of Loss Coefficient: 0.1 C_{ax} downstream (Baseline vs. AO - with coolant)

Chapter 4: Aerodynamic Measurements – Discrete Hole Cooling

4.1 Overview

Discrete holes were implemented for film cooling on the endwall surface on both the Baseline and AO contoured geometries. The purpose of was to investigate hoe the aerodynamic performance affected with the coolant injection. The upstream leakage slot design was retained. However, it should be made clear that for all the upcoming results, discrete hole blowing and purge cooling were not performed in conjunction. The coolant line to the plenum of the leakage slot was closed off. The cavity was not sealed or blocked off in any way during these experiments allowing for mainstream injection into the cavity. Just as in the upstream leakage slot, experiments were conducted for both blowing and non-blowing cases to further understand what underlying features that may arise as a result of the endwall surface changes. The layouts of the holes are with respect to the passage flow streamlines. The discrete holes were position with both geometries in mind. That being said, the considerations for passage flow performance for both geometries were determined and a design that complimented both geometries was implemented. There were a set of three rows of holes placed on the surface. The first row being closest to the pressure side of the airfoil consisted of seven holes, followed by a row of eight, and then finally a row of nine.

4.2 **Effect of Holes - with Holes (No Cooling) vs. w/out Holes (Baseline & AO)**

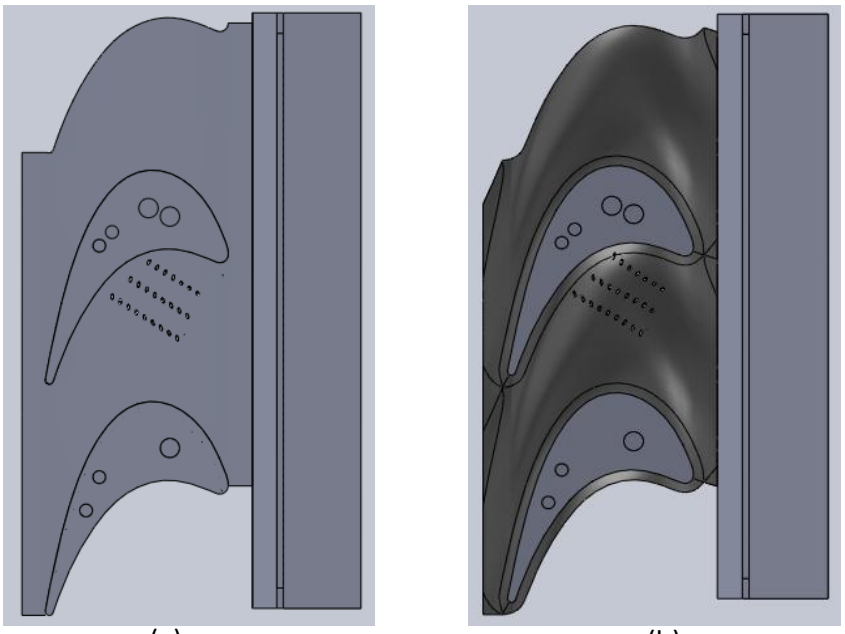

Figure 4.1: Baseline and AO contoured geometries with discrete holes (In Presence of Slot).

It is important to compare how the addition of discrete holes to the design affects the passage flow before any cases with blowing are explored. The discrete holes experienced mainstream flow entering the discrete holes' cavity and recirculating. This was observed in both plenum static pressure measurements as well as through the infrared imaging used to conduct the heat transfer experiments. The flow seems to enter in the first two rows of holes and leaks out of the third row. This flow behavior when no injection is present and when injection is present affects the endwall and secondary flow of the passage in such a way that it certainly changes the loss profiles seen for the case of no discrete holes with an upstream purge slot. The discrete holes affect spanwise losses and especially the shape and magnitude of the passage vortex cores.

The Baseline and AO geometry have a decrease in the mixed out losses throughout the span. The most noticeable trend in comparing Figure 4.2 (a) & (b) is that the passage vortex core

looks to be slightly reduced in strength and pull down in the spanwise region. The ingress with leakage may be delaying the meeting time of the cavity vortex with the suction side vortex delaying lift off. Despite any reduction (baseline) or increase (AO) in passage vortex strength, the addition of holes increases the losses for the slot geometry by ~4% and ~3% for the baseline and AO geometries, respectively.

The same trend may be true for the AO contoured case where the passage vortex core looks slightly elongated like in the Baseline case, but not to the same extent. The flow ingress maybe altering the pressure variation along the endwall allowing the contouring to behave more as it did without the slot. More notable in Figure 4.3 (a) & (b) is that the intensity of the passage vortex seems to have increased slightly. These variations in intensity and center locations of the vortex being so close to the edge of view make any concrete conclusions difficult. One thing for sure is that the pressure gradient across the passage directly influences the direction and magnitude of the passage vortex. The altered flow structures near the endwall may be affecting the secondary flow enough to see this change. Though there isn't any blowing through the holes the passage cross flow intensifies the AO geometry passage vortex.

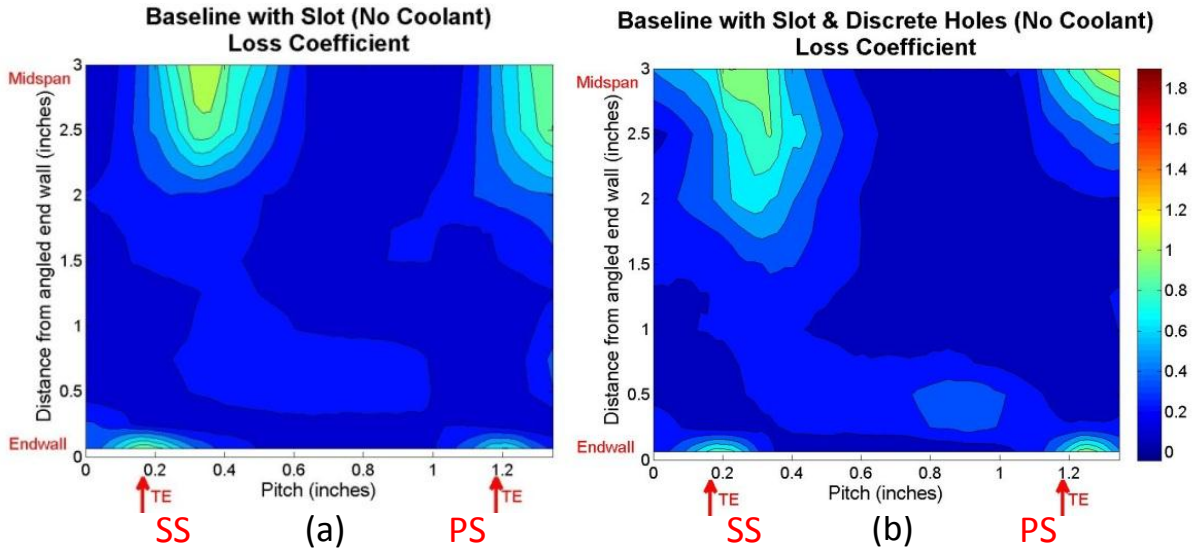

Figure 4.2: Baseline endwall Loss Coefficient at 0.1 C_{ax} downstream of the trailing edge (a) with and (b) without discrete hole (with upstream slot), 0% MFR

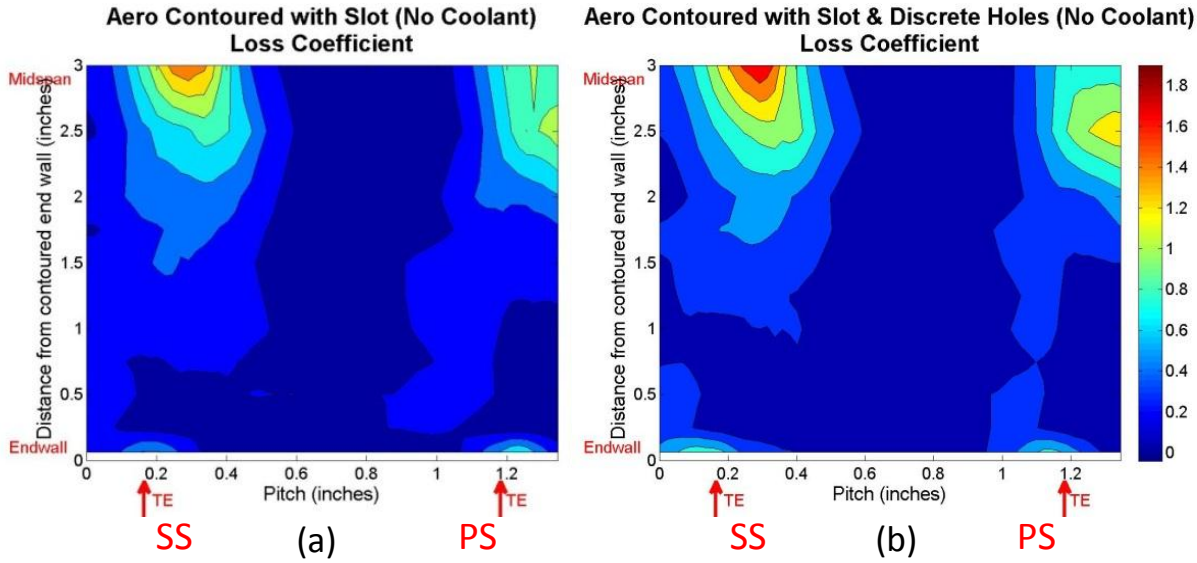

Figure 4.3: AO contoured Loss Coefficient at 0.1 C_{ax} downstream of the trailing edge (a) with and (b) without discrete hole (with upstream slot), 0% MFR.

What can be said with some certainty is that the addition of discrete holes has negligible effects on the overall losses for the Baseline geometry, whereas the losses seen with the Aero contoured cases increase by approximately 14% for the addition of holes on the endwall.

4.3 Effect of Coolant Injection and Contouring

It was previously observed that the upstream leakage slot was the dominating factor in altering the secondary flow structures and inducing higher losses without blowing. With endwall hole coolant injection (0.25% MFR), it was clear that the contoured endwall geometry was able to yield beneficial results by decreasing some of the losses incurred due to the presence of the slot. There was a reasonable increase in performance for the baseline of about 2.5% reduction in losses, while the AO geometry saw only ~½% reduction in area averaged losses. It is important to stress that for both geometries losses did increase due to the presence of the slot and increased further for the 1% MFR blowing case. In the following sections the effects of the discrete holes for with and without blowing cases will be discussed in detail in the following sections.

4.3.1 Baseline with and without Discrete Hole Blowing

The coolant injection of the discrete holes had a 0.25% MFR. Given the low MFR no significant increase or reduction in losses were expected. From a quick glance it would seem that that passage vortex intensity has decreased slightly with the injection of coolant. The vortex in the upper right corner of the discrete hole blowing case seems to have been reduced enough to where it is almost no longer in our field of view.

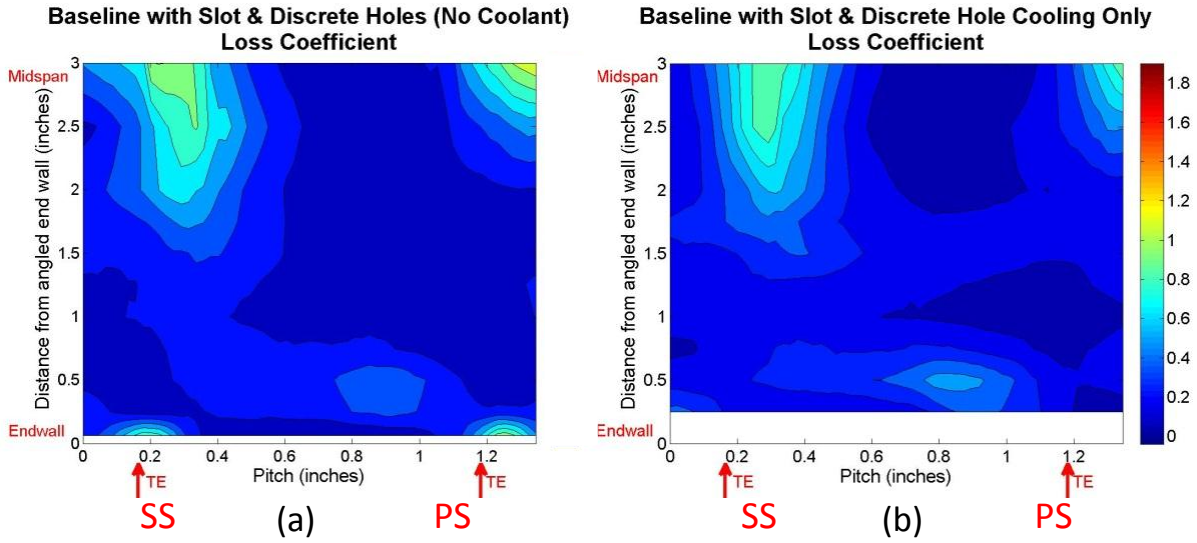

Figure 4.4: Baseline Loss Coefficient at 0.1 C_{ax} downstream of the trailing edge (a) with and (b) without discrete holes (with upstream slot); 0% vs. 0.25% MFR

The most notable trend is that the spanwise losses throughout the passage decreased with the addition of holes and has seen an minute increase due to the coolant injection. This indicates that the ingress may positively affect the blade passage pressure gradient decreasing the adverse secondary flow development. In Figure 4.4 (b), the region near the endwall had data points that are believed to be non-representative of the actual flow and were removed. The area average losses decrease by about ~2.5% with the addition of blowing through the discrete holes.

4.3.2 **AO with and without Discrete Hole Blowing**

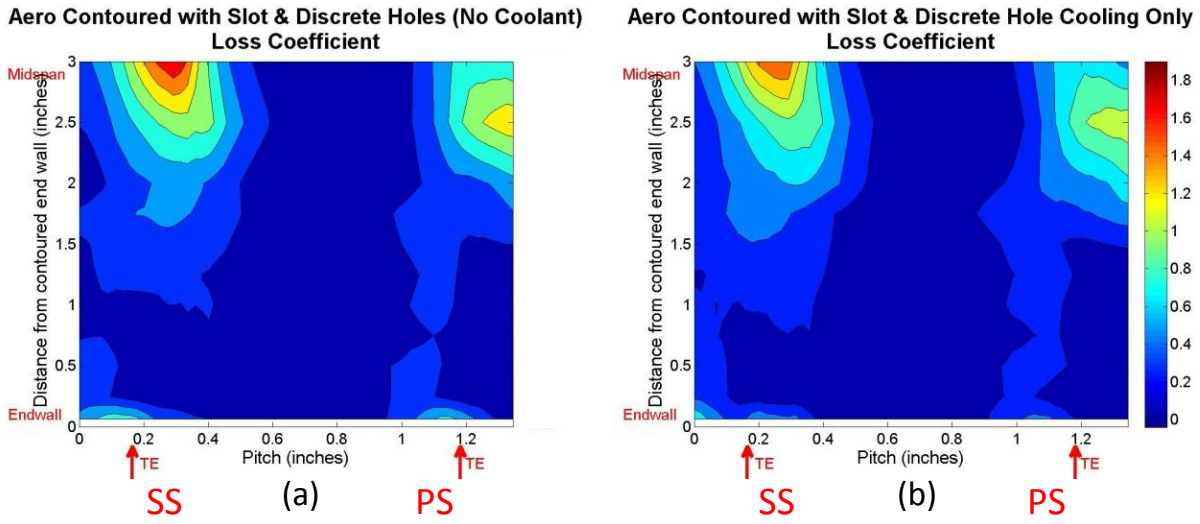

Figure 4.5: Baseline with and without discrete holes (with upstream slot) Loss Coefficient at 0.1 C_{ax} downstream of the trailing edge; 0% vs. 0.25% MFR

Similar to the Baseline case the AO contoured geometry sees a reduction in losses for coolant injection, approximately a ½% in area averaged losses. The losses throughout the span seem relatively unaffected as it was with the baseline geometry, though the passage vortices had decreased in magnitude with the 0.25% MFR. The significant change in area average losses from the non-blowing to blowing case is believed to be due to how the static pressure along the endwall is distributed. The contouring along with the discrete holes affects the passage pressure gradient directing the passage vortex along the endwall more similar to how it was observed and designed to do with the no slot case. The contouring is able to carry the passage vortex along the endwall, meeting up with the suction side vortex at a later time thereby reducing its intensity. The coolant injection also appears to also reduce the strength of the corner vortices near the endwall.

4.3.3 **Effect of Endwall Contouring (Baseline vs. Aero - with and without Coolant)**

The two figures below, Figure 4.7 and Figure 4.9, make it evident of that which was just discussed. The endwall loss coefficient for the AO contoured geometry is not significantly affected between the blowing and non-blowing cases. From about 0.1 normalized span to midspan the Baseline geometry yields lower pitchwise average losses than compared to the AO contoured for the discrete hole no blowing case. The loss values for the AO geometry are relatively close to the Baseline up until about 0.35 normalized span where the average pitchwise loss coefficient increases more steeply due to the higher intensity passage vortex. In comparing the two cases the AO contoured has 14% higher losses.

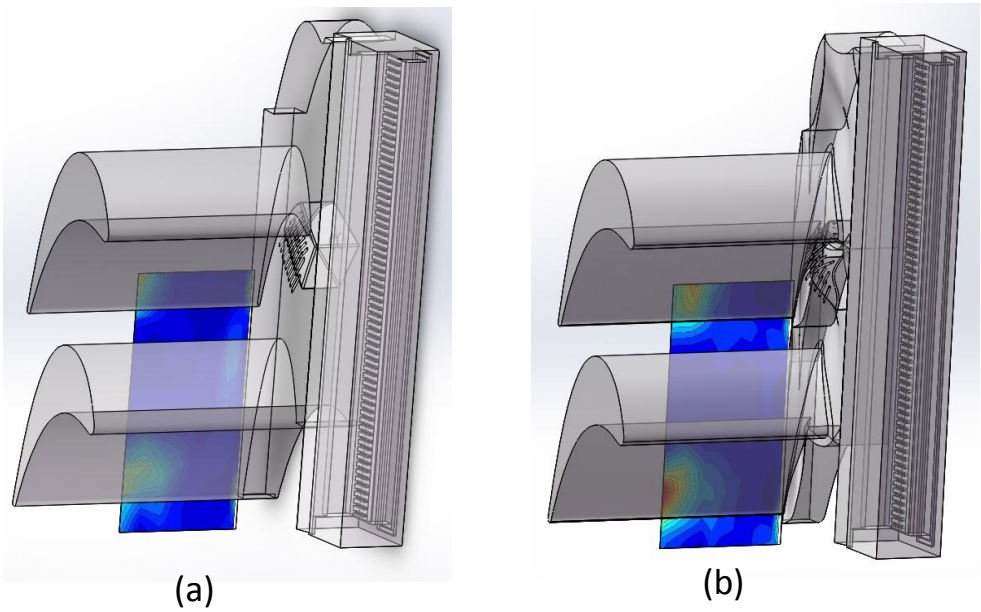

Figure 4.6: Baseline and AO contoured geometries with discrete holes (0% Purge)

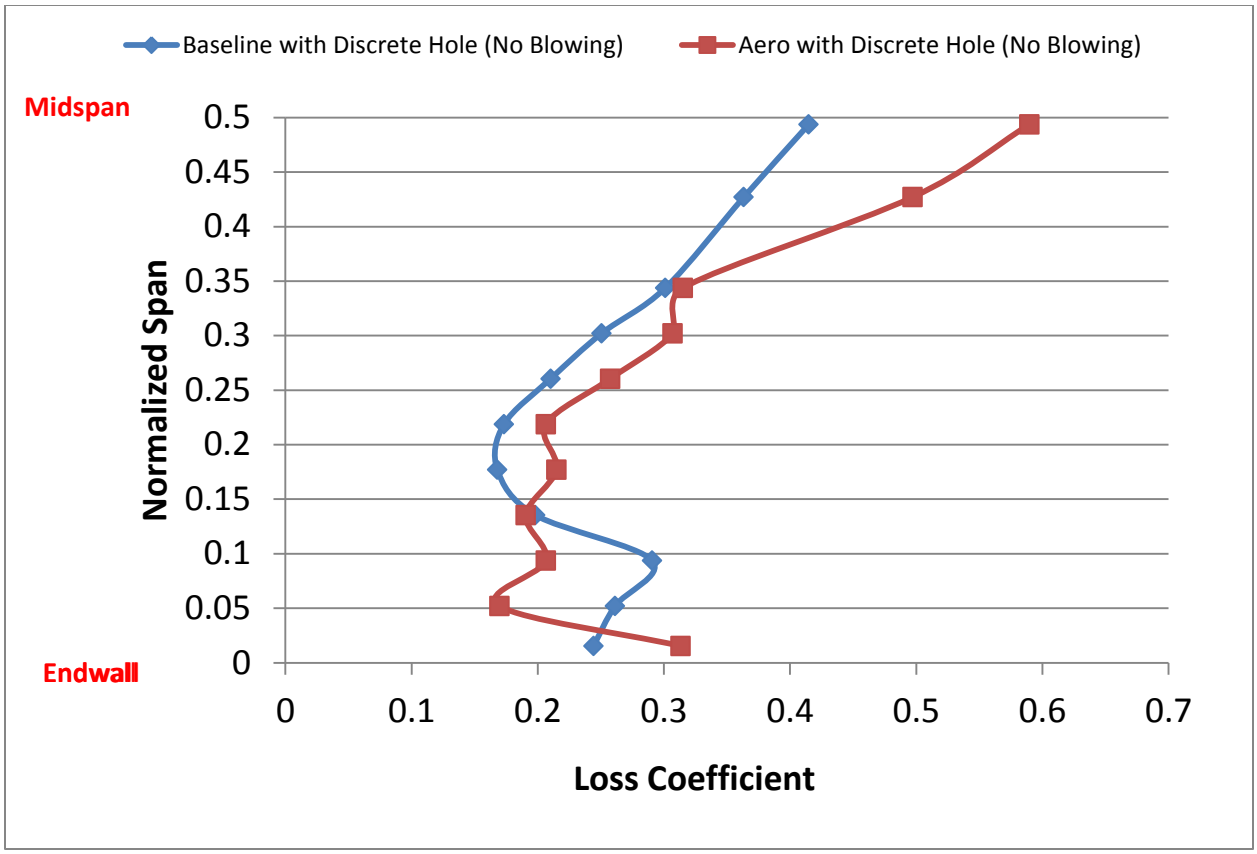

Figure 4.7: Spanwise variation of Loss Coefficient: 0.1 C_{ax} downstream Baseline vs. AO Contoured Discrete Hole (No Blowing)

When discrete hole blowing is introduced, the loss trend near the endwall for the Baseline case was removed due to the presence of non-realistic values. At about 0.25 normalized span the average pitchwise loss coefficients are relatively linear in increasing losses. The AO contoured geometry has a much steeper trend to a loss coefficient of about 0.52 at midspan. When comparing the loss coefficients for the same averaged area for the Baseline and Aero geometries with coolant holes with blowing, the Baseline geometry performs 16% better than the Aero contoured geometry.

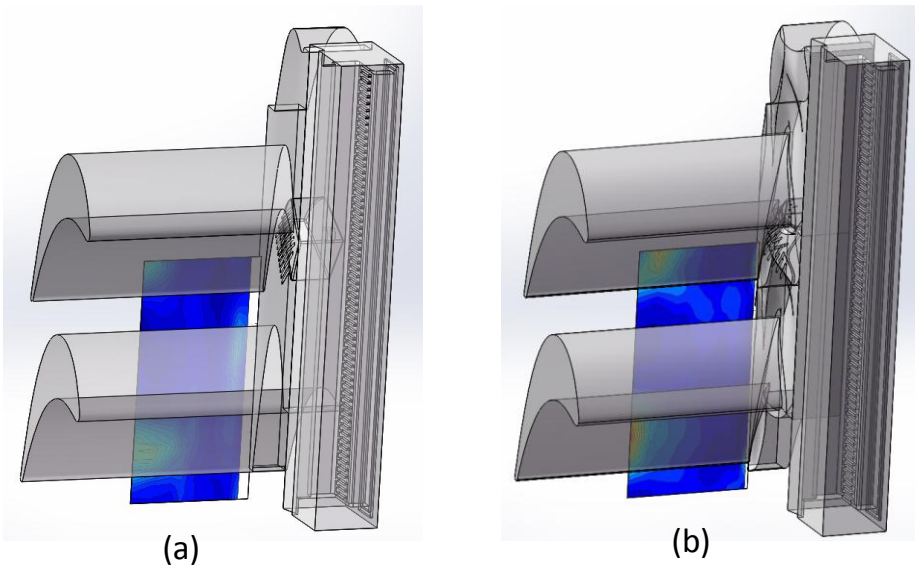

Figure 4.8: Baseline and AO contoured geometries with discrete holes (0.25% Purge)

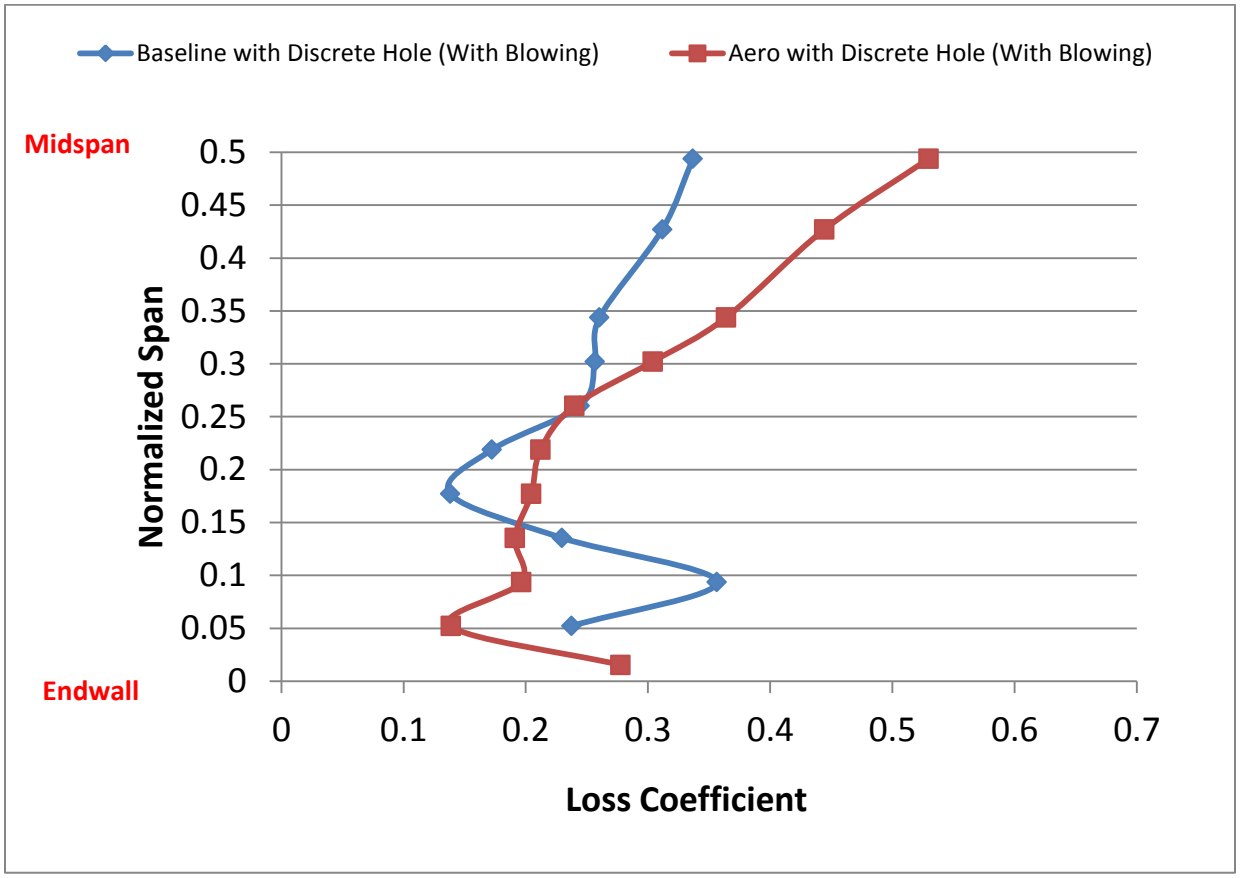

Figure 4.9: Spanwise variation of Loss Coefficient: 0.1 C_{ax} downstream Baseline vs. AO Contoured Discrete Hole (With Blowing)

It has been a continuing trend that the Baseline geometry yields significantly higher losses near the endwall compared to the AO contoured geometry. The addition of the slot exaggerated this and then the addition of the purge slot cooling increased it further. Interestingly, the case of discrete holes and no blowing in the presence of a purge slot gave it values that were similar to those seen without a slot.

It is then in the case with no blowing the ingress aides in creating similar conditions where the endwall pressure gradient directs the passage/cavity vortex along the endwall longer before it meets with the suction side vortex. This feature significantly lowers losses throughout the span and at midspan than compared to the with slot cases. As for the AO contoured case, the flow from the last row coolant hole injection is being rolled up into the cavity vortex slightly intensifying the vortex. The greatest factor is that the AO contoured geometry was optimized for when mainstream flow passed through without the presence of an upstream leakage slot, discrete holes, and any form of non-blowing or blowing cases. Therefore it is believed that due to the ingress and coolant injection cases the endwall stagnation pressure and secondary flows affect the passage pressure gradient in such a way that losses increase compared to its original no slot case.

Chapter 5: Summary and Conclusions

In Table 5.1, the calculated percent differences for the two geometries are presented. The values are average loss coefficient values that were calculated throughout the pitch and span between the two trailing edges of the blades. This average is performed at every spanwise location by multiplying the average of the losses pitchwise by the distance between two successive points. This distance is measured from the endwall considering it is at a position of 0 inches. The spanwise measurements were taken at ¼ inch increments up to the last points near the midspan which were incremented at ½ inch intervals. It is due to this uneven spacing that the distance weighted average was necessary instead of a simple line average. The distance weighted average was performed for two sets of runs, the first set and a repeatability set. These distance weighted area averaged loss coefficients were averaged between the two sets to give the values presented below.

Table 5.1: Area Average Loss Coefficient Summary

	TE to TE Distance Weighted Averaged Loss Coefficients			
		Baseline	***Aero***	***Percent Difference***
No Blowing	***No Slot***	0.270	0.249	8%
	With Slot	0.270	0.283	-5%
	With Discrete Hole	0.277	0.315	-14%
With Blowing	***With Slot***	0.280	0.292	-4%
	With Discrete Hole	0.270	0.313	-16%

Data Set without Near Endwall Losses

An investigation into the aerodynamic performance of two geometries was performed. The two geometries, the Baseline which has an angled endwall geometry with a 13^0 angle and an Aero Optimized endwall that was selected due to its decreased losses seen from the previous study of Abraham and Panchal [31, 32]. These two geometries were then fitted with an upstream

leakage slot design for purge cooling on the endwall. Afterward, discrete hole coolant injection was implemented into the design for further HTC reduction. While observing the enhancements gained through a decreased endwall heat transfer, the aerodynamic performance was a source of interest to ensure a robust design. The area averaged losses from trailing edge to trailing edge was determined and summarized in Table 1. Take note that the area averaged losses for the Baseline discrete holes with blowing had data points near the endwall removed due to unrealistic results. In order to compare the same areas of interest the same was done for the Aero contoured with discrete holes blowing case. However, the value of the area averaged loss coefficient does not change considerably. The value changes by a thousandth of a decimal point.

In almost all cases the baseline geometry performed better than the Aero contoured geometry. The only time in which the AO contoured geometry performed favorably is the case without any film cooling techniques implemented. Any other time, the baseline geometry yielded lower losses than the AO for their respective cases of no slot, with slot (no blowing), with slot (with blowing), and finally discrete holes in the presence of slot (with blowing). The upstream slot and the coolant alter the inlet boundary layer affecting the secondary flow development throughout the passage. Similar instances were recorded by Biesinger and Gregory-Smith and Gao et al [12, 16]. With every new feature added to the design, both geometries incurred higher area average losses at 0.1 C_{ax} downstream of the trailing edge. In general, the losses from the highest area average losses to lowest are the geometry with discrete holes in the presence of slot, with slot, and then no slot case. The no slot case does still yield the lowest loses. In comparing the cases with discrete holes and without discrete holes, the secondary flow is altered. The presence of the discrete holes on the endwall and with and without coolant reduced the strength of the passage vortex for the flat endwall case and increased the strength for the aero contoured

case. Friedrichs et al. and Knost et al. [15, 28] saw that the discrete hole coolant injection in high static pressure regions produced a reduction in losses.

The upstream leakage slot is the driving factor for new secondary flow development and increased losses while any coolant blowing amplifies these effects. The presence of the slot clearly affected the path by affecting the passage pressure gradient and when the passage vortex lifted from the wall. In the work Knost et al. [15], they also found that the position of the slot could cause the early development of the passage vortex. Blanco et al. and Colban et al. [9, 11] more specifically looked at the effects of a backward facing step and found the same results show here that the slot reduces the strength of the passage vortex and suction side corner vortices. The development of a vortex originating from the slot and the early lift off of the passage vortex from the endwall caused the passage vortex location to migrate further into the midspan which was similarly measured by Blanco et al. [11].

The only advantage the AO contoured geometry seems to have over the baseline is that it seems to control and provide similar losses near the endwall for each film and non-film cooling cases. The baseline geometry has radical variations in the losses along the endwall. Despite this the overall performance with respect to losses is better for the flat endwall case. Duden et al. [19] similarly didn't yield any major improvements in aerodynamic loss reduction for high turning airfoils. Where just as in this case, Taremi et al. found that at transonic operating conditions and for high turning angle airfoils a reduction in losses in negligible in using a contoured endwall.

The results here, have been looked at microscopically, but from a macroscopic viewpoint the losses between the no slot, with slot, and with slot and discrete hole cases are negligible. Taking the lowest area average loss coefficient of 0.270 and the highest 0.315 from Table 5.1 and referring back to Figure 2.17 the amount of uncertainty in measurement is about 3.4% to 3.5%.

The high certainty in results and small difference between the losses for each case shows that endwall contouring isn't worth the cost and the film cooling techniques on the heat transfer yield beneficial results with a minimum impact on losses under transonic conditions. Demonstrating that higher turbine inlet temperatures could possibly be achieved with added film cooling without a significant impact on turbine aerodynamic performance, thereby increasing the life and efficiency of gas turbine engines.

5.1 **Experimental Improvements**

In performing the loss measurement experiments, it brought to mind areas of possible improvement. First off, to avoid any possible data skewing, it would be best that all possible spanwise measurements were taken at evenly space increments throughout the passage in order to have higher resolution at areas of interest. The passage vortices in the contour plots are the most interpolated due to this spacing. The equal spacing will also alleviate any concerns of numerical weigh on the spanwise losses as well as give a more accurate trend for the flow near midspan.

It is being looked into for future projects, but full span traverse measurements would be optimal. Though time constraints make this difficult through repeatability, but it will give more understanding of the passage flow characteristics and may allow us to see the full view of the passage vortex, for cases such as the ones presented here where the passage vortex migrated further to the midspan due to the geometry.

References

[1] Panchal, K., Abraham, S., Ekkad, S. V., Ng, W., Brown, B. J., and Malandra, A., 2011, "Investigation of Effect of End Wall Contouring Methods on a Transonic Turbine Blade Passage," ASME Conference Proceedings, 2011(54679), pp. 523-534.

[2] Rodger, P., Sjolander, S., and Moustapha, S., "Establishing two-dimensional flow in a large-scale planar turbine cascade," Proc. AIAA, SAE, ASME, and ASEE, Joint Propulsion Conference and Exhibit, 28 th, Nashville, TN, p. 1992.

[3] Abraham, S., Panchal, K., Ekkad, S. V., Ng, W., Lohaus, A. S., and Malandra, A., 2012, "Measurement of Aerodynamic Losses for Turbine Airfoil Cascades with Varying Pitch, Operating Under Transonic Conditions."

[4] Zoric, T., Popovic, I., Sjolander, S. A., Praisner, T., and Grover, E., 2007, "Comparative Investigation of Three Highly Loaded LP Turbine Airfoils: Part I --- Measured Profile and Secondary Losses at Design Incidence," ASME Conference Proceedings, 2007(47950), pp. 621-630.

[5] Zoric, T., Popovic, I., Sjolander, S. A., Praisner, T., and Grover, E., 2007, "Comparative Investigation of Three Highly Loaded LP Turbine Airfoils: Part II --- Measured Profile and Secondary Losses at Off-Design Incidence," ASME Conference Proceedings, 2007(47950), pp. 631-638.

[6] Blair, M. F., 1974, "An Experimental Study of Heat Transfer and Film Cooling on Large-Scale Turbine Endwalls," Journal of Heat Transfer, 96(4), pp. 524-529.

[7] Armaly, B., Durst, F., Pereira, J., and Schonung, B., 1983, "Experimental and theoretical investigation of backward-facing step flow," J. Fluid Mech, 127(473), p. 20.

[8] Papa, M., Srinivasan, V., and Goldstein, R. J., 2010, "Film Cooling Effect of Rotor-Stator Purge Flow on Endwall Heat/Mass Transfer," ASME Conference Proceedings, 2010(43994), pp. 1729-1738.

[9] Colban, W., Thole, K., and Zess, G., 2003, "Combustor Turbine Interface Studies-Part 1: Endwall Effectiveness Measurements," Transactions of the ASME-T-Journal of Turbomachinery, 125(2), pp. 193-202.

[10] Colban, W., Lethander, A., Thole, K., and Zess, G., 2003, "Combustor turbine interface studies: Part 2: Flow and thermal field measurements," Journal of turbomachinery, 125(2), pp. 203-209.

[11] Blanco, E. d. l. R., Hodson, H. P., and Vazquez, R., 2006, "Effect of the Leakage Flows and the Upstream Platform Geometry on the Endwall Flows of a Turbine Cascade," ASME Conference Proceedings, 2006(4241X), pp. 733-744.

[12] Biesinger, T. E., and Gregory-Smith, D. G., "Reduction in secondary flows and losses in a turbine cascade by upstream boundary layer blowing," Proc. ASME, International Gas Turbine and Aeroengine Congress and Exposition, Cincinnati, OH.

[13] Chyu, M. K., 2001, "Heat Transfer near Turbine Nozzle Endwall," Annals of the New York Academy of Sciences, 934(1), pp. 27-36.

[14] Paniagua, G., Denos, R., and Almeida, S., "Effect of the hub endwall cavity flow on the flow-field of a transonic high-pressure turbine," Journal of turbomachinery, 126(4), pp. 578-586.

[15] Knost, D. G., Thole, K. A., and Duggleby, A., 2009, "Evaluating a Three-Dimensional Slot Design for the Combustor-Turbine Interface," GT2009-60168.

[16] Gao, Z., Narzary, D. P., Mhetras, S., and Han, J. C., 2012, Upstream Vortex Effect on Turbine Platform Film Cooling with Typical Purge Flow, American Institute of Aeronautics and Astronautics, Reston, VA, United States.

[17] Morris, A. W. H., and Hoare, R. G., 1975, "Secondary loss measurements in a cascade of turbine blades with meridional wall profiling," pp. ASME Paper 75-WA/GT-13.

[18] Dossena, V., Perdichizzi, A., and Savini, M., 1999, The influence of endwall contouring on the performance of a turbine nozzle guide vane, American Society of Mechanical Engineers, New York, NY, United States.

[19] Duden, A., Raab, I., and Fottner, L., 1999, Controlling the secondary flow in a turbine cascade by three-dimensional airfoil design and endwall contouring, American Society of Mechanical Engineers, New York, NY, United States.

[20] Burd, S. W., and Simon, T. W., 2000, Flow measurements in a nozzle guide vane passage with a low aspect ratio and endwall contouring, American Society of Mechanical Engineers, New York, NY, United States.

[21] Hartland, J. C., Gregory-Smith, D. G., Harvey, N. W., and Rose, M. G., 2000, "Nonaxisymmetric turbine end wall design: Part II -- Experimental validation," Journal Name: Journal of Turbomachinery; Journal Volume: 122; Journal Issue: 2; Conference: 44th International Gas Turbine and Aeroengine Congress and Exhibition, Indianapolis, IN (US), 06/07/1999--06/10/1999; Other Information: PBD: Apr 2000, pp. Medium: X; Size: page(s) 286-293.

[22] Nagle, M. G., and Baier, R.-D., 2005, Experimentally verified numerical optimization of a three-dimensional parametrized turbine vane with nonaxisymmetric end walls, American Society of Mechanical Engineers, New York, NY, United States.

[23] Praisner, T. J., Allen-Bradley, E., Grover, E. A., Knezevici, D. C., and Sjolander, S. A., 2007, "Application of Non-Axisymmetric Endwall Contouring to Conventional and High-Lift Turbine Airfoils," ASME Conference Proceedings, 2007(47950), pp. 653-661.

[24] Ross, G., Gazi, M., and Sumanta, A., 2007, "Aerodynamic Measurements in a Linear Turbine Blade Passage With Three-Dimensional Endwall Contouring," ASME Conference Proceedings, 2007(47950), pp. 855-865

[25] Snedden, G., Dunn, D., Ingram, G., and Gregory-Smith, D., 2009, "The Application of Non-Axisymmetric Endwall Contouring in a Single Stage, Rotating Turbine," ASME Conference Proceedings, 2009(48883), pp. 831-840.

[26] Kopper, F. C., Milanot, R., and Vancot, M., 1981, "Experimental Investigation of Endwall Profiling in a Turbine Vane Cascade," AIAA Journal, 19(8), pp. 1033-1040.

[27] Taremi, F., Sjolander, S. A., and Praisner, T. J., 2011, "Application of Endwall Contouring to Transonic Turbine Cascades: Experimental Measurements at Design Conditions," ASME Conference Proceedings, 2011(54679), pp. 911-922

[28] Friedrichs, S., Hodson, H., and Dawes, W., 1997, "Aerodynamic aspects of endwall film-cooling," Transactions-American Society of Mechianical Engineers Journal of Turbomachinery, 119, pp. 786-793.

[29] Kost, F., and Nicklas, M., 2001, "Film-Cooled Turbine Endwall in a Transonic Flow Field: Part I---Aerodynamic Measurements," Journal of turbomachinery, 123(4), pp. 709-719.

[30] Abraham, S., Panchal, K., Ekkad, S. V., Ng, W. F., Lohaus, A. S., and Malandra, A., 2012, "Effect of Endwall Contouring on a Transonic Turbine Blade Passage: Part 1 – Aerodynamic Performance," ASME Conference Proceedings(ASME Paper No. GT2012-68425).

[31] Abraham, S., 2011, "Aerodynamic performance of high turning airfoils and the effect

of endwall contouring on turbine performance," Doctor of Philosophy, Virginia Polytechnic Institute and State University, Blacksburg, Virginia.

[32] Panchal, K., 2011, "Development of a Robust Numerical Optimization Methodology for Turbine Endwalls and Effect of Endwall Contouring on Turbine Passage Performance," Doctor of Philosophy, Virginia Polytechnic Institute and State University, Blacksburg, Virginia.

[33] Ligrani, P. M., Singer, B. A., and Baun, L. R., 2000, "Miniature five-hole pressure probe for measurement of three mean velocity components in low-speed flows," Journal of Physics E: Scientific Instruments, 22(10), p. 868.

[34] Main, A. J., Day, C. R. B., Lock, G. D., and Oldfield, M. L. G., 1996, "Calibration of a four-hole pyramid probe and area traverse measurements in a short-duration transonic turbine cascade tunnel," Experiments in fluids, 21(4), pp. 302-311.

[35] Pisasale, A. J., and Ahmed, N. A., 2002, "Theoretical calibration for highly three-dimensional low-speed flows of a five-hole probe," Measurement Science and Technology, 13(7), p. 1100.

[36] Kline, S. J., and McClintock, F., 1953, "Describing uncertainties in single-sample experiments," Mechanical engineering, 75(1), pp. 3-8.

[37] Blanco, E. d. l. R., Hodson, H. P., and Vazquez, R., 2005, "Effects of Upstream Platform Geometry on the Endwall Flows of a Turbine Cascade," ASME Conference Proceedings, 2005(47306), pp. 735-745.

[38] Takeishi, K., Matsuura, M., Aoki, S., and Sato, T., 1989, "An experimental study of heat transfer and film cooling on low aspect ratio turbine nozzles," American Society of Mechanical Engineers, 1.

[39] Lampart, P., "Investigation of endwall flows and losses in axial turbines. Part I. Formation of endwall flows and losses."

[40] Langston, L. S., 2006, "Secondary flows in axial turbines—a review," Annals of the New York Academy of Sciences, 934(1), pp. 11-26.

Appendix A – 5 Hole Probe Pressure Profile Matching and Cropping

```
clc
clear all
close all

%%
% This is for allocating column locations from data files.

% The numbers corresponds to the ports on the pressure system and may need
% to be updated with individual setups
Pitot_Probe_Total_Port=4;
Static_Pressure_Static_Port=5;
P1_Port=6;
P2_Port=7;
P3_Port=8;
P4_Port=9;
P5_Port=10;

% The numbers corresponds to the channels from the NI-DAQ system and may need
% to be updated with individual setups
Total_Pressure_Signal=6;
Traverse_Signal=7;
%%
prompt={'Atmospheric Pressure:', ...
    'Run #:'};
dlg_title = 'Inputs for Plot Matching';
num_lines = 1;
answer = inputdlg(prompt,dlg_title,num_lines);
d=str2num(answer{2});

% Determines the current data: Not currently used.
s = datestr (now, 'mm_dd_yyyy');

% Prompts you to select data files to be used.
% Select Pressure Data File from Netscanner converted to CSV file
[File Path] = uigetfile('*.xls','Select Pressure File');
excelFilename1 = [Path File];
cd(Path)
% Select labview .lvm file with traverse movement trace
[File Path] = uigetfile('*.xls','Select NI-DAQ File');
excelFilename2 = [Path File];

% Takes the data from the selected data files and inputs them into arrays
psi_data=xlsread(excelFilename1);
traverse_data_load=xlsread(excelFilename2);
traverse_data=traverse_data_load(23:322,:);
```

```
traverse_data(:,Total_Pressure_Signal)=traverse_data(:,Total_Pressure_Signal)-
traverse_data(1,Total_Pressure_Signal);

% Pulls the first Cell in the name structure of the files.
% extract the date (it's returned in a cell array
excel_list = dir('Traverse*.xls');
oldFileName =  excel_list(1,1).name;
theDate = regexp(oldFileName,'(\d{2}_\d{2}_\d{4})','match');
date_of_data = sprintf('%s',theDate{1});
savename=sprintf('Run_%d_testdata_%s.xls',d, date_of_data);

% Extracts Total pressure profile read from the pressure transducer
% Extracts voltage signal indicating the traverse is moving or not (0=not
% moving 5V=moving) looks like a square wave
P_total=traverse_data(:,Total_Pressure_Signal);  % Column 6 is for the pressure
Traverse_on_off=traverse_data(:,Traverse_Signal); % column 7 is location of the data

% Atmospheric Pressure
P_atm=str2num(answer{1});

%% Creating more manageable arrays of data
a=1;
b=1;
c=1;

%First column is time, all others are the pressure channels
data_2675(1:1000,1:17)=0;
data_2686(1:1000,1:17)=0;
data_2699(1:1000,1:17)=0;
for x=12:size(psi_data,1)
   if (psi_data(x,3)==2675)
      data_2675(a,1)=psi_data(x,1);
      data_2675(a,2:17)=psi_data(x,7:22);
      a=a+1;
   elseif(psi_data(x,3)==2686)
      data_2686(b,1)=psi_data(x,1);
      data_2686(b,2:17)=psi_data(x,7:22);
      b=b+1;
   elseif(psi_data(x,3)==2699)
      data_2699(c,1)=psi_data(x,1);
      data_2699(c,2:17)=psi_data(x,7:22);
      c=c+1;
   end
end
a=a-1;
b=b-1;
```

```
c=c-1;
%% Determining time shift of traverse data
A=1;
D=1;
lim=0.4;
while (data_2675(A,4)<lim || traverse_data(D,6)<lim)  %column 6 is where the pressure
transducer was recorded
   if data_2675(A,4)<lim
      A=A+1;
   end
   if traverse_data(D,6)<lim
      D=D+1;
   end
end
A=A-1;
D=D-1;

adj_data_2675_time=data_2675(A:A+1,1);
adj_data_2675_pressure=data_2675(A:A+1,4);

adj_traverse_data_time=traverse_data(D:D+1,1);
adj_traverse_data_pressure=traverse_data(D:D+1,6);

yi1 = interp1(adj_data_2675_pressure, adj_data_2675_time, 0.4);
yi2 = interp1(adj_traverse_data_pressure, adj_traverse_data_time, 0.4);

tshift=yi2-yi1;

%%
% Finds when the travels moved, indexes that location in order to extract
% appropriate data
for i=1:size(traverse_data,1)
   if abs(traverse_data(i,7)>4.99)
      p=i;
      break
   end
end

q=p+60;

psi_range_2675_traverse=data_2675(p:q,:);
psi_range_2686_traverse=data_2686(p:q,:);
psi_range_2699_traverse=data_2699(p:q,:);
traverse_range_traverse=traverse_data(p:q,:);
points_x1=1:61;
```

```
%Pitot Probe
pt_in=psi_range_2675_traverse(:,Pitot_Probe_Total_Port);
ps_in=psi_range_2675_traverse(:,Static_Pressure_Static_Port);

% Five Hole Probe
p1=psi_range_2675_traverse(:,P1_Port);
p2=psi_range_2675_traverse(:,P2_Port);
p3=psi_range_2675_traverse(:,P3_Port);
p4=psi_range_2675_traverse(:,P4_Port);
p5=psi_range_2675_traverse(:,P5_Port);

Output_data_traverse(1,1:q-p+1)=pt_in;
Output_data_traverse(2,1:q-p+1)=ps_in;
Output_data_traverse(3,1:q-p+1)=p1;
Output_data_traverse(4,1:q-p+1)=p2;
Output_data_traverse(5,1:q-p+1)=p3;
Output_data_traverse(6,1:q-p+1)=p4;
Output_data_traverse(7,1:q-p+1)=p5;

excel_list = dir('Traverse*.xls');
oldFileName =  excel_list(1,1).name;
% Pulls the first Cell in the name structure of the files.
% extract the date (it's returned in a cell array
theDate = regexp(oldFileName,'(\d{2}_\d{2}_\d{4})','match');
date_of_data = sprintf('%s',theDate{1});

colnames1 = {'P1','P2','P3','P4','P5'};
colnames2 = {'Pt_in','Ps_in'};
colnames3 = {'Atmospheric Pressure'};

% Writes the cropped pressure data to an excel spreadsheet after p
% Pressure matching of the two tunnel profiles.
xlswrite(savename, colnames1, 'sheet1','A1:E1');
xlswrite(savename, Output_data_traverse(3:7,:)', 'sheet1','A2:E62');

xlswrite(savename, colnames2, 'sheet2','A1:B1');
xlswrite(savename, Output_data_traverse(1,:)', 'sheet2','A2:A62');

xlswrite(savename, colnames3, 'sheet3','B1');
xlswrite(savename, P_atm, 'sheet3');

% Creates Directories in the Path Location for Saved Plots
[Path]=pwd;
mkdir([Path,'\Plots'])
mkdir([Path,'\Plots\Figures'])
mkdir([Path,'\Plots\JPEGS'])
```

```
figures=[Path, '\Plots\Figures\'];
jpegs=[Path, '\Plots\JPEGS\'];

%% Plotting
figure(1)
hold on
plot(data_2675(1:a,1),data_2675(1:a,4), 'b')
plot(traverse_data(:,1),traverse_data(:,6), 'g')
plot(traverse_data(:,1),traverse_data(:,7), 'r')
xlabel('Time (s)')
ylabel('Response')
title('Skewed Pressure Timing')
set(gcf, 'Position', [200 100 800 600])
set(gca,'FontSize',14)
h_xlabel = get(gca,'XLabel');
set(h_xlabel,'FontSize',16);
h_ylabel = get(gca,'yLabel');
set(h_ylabel,'FontSize',16);
h_title = get(gca,'title');
set(h_title,'FontSize',20, 'FontWeight', 'bold');
set(gcf,'Color',[0.82,0.83,0.78])
set(text,'fontweight','bold');
legend('Pressure Scanner', 'Transducer', 'Traverse','Location', 'Northeast')

figure(1)
hold on
plot(data_2675(1:a,1),data_2675(1:a,4), 'b')
plot(traverse_data(:,1)-tshift,traverse_data(:,6), 'g')
plot(traverse_data(:,1)-tshift,traverse_data(:,7), 'r')
xlabel('Time (s)')
ylabel('Response')
title('Pressure Response Matching')
set(gcf, 'Position', [200 100 800 600])
set(gca,'FontSize',14)
h_xlabel = get(gca,'XLabel');
set(h_xlabel,'FontSize',16);
h_ylabel = get(gca,'yLabel');
set(h_ylabel,'FontSize',16);
h_title = get(gca,'title');
set(h_title,'FontSize',20, 'FontWeight', 'bold');
set(gcf,'Color',[0.82,0.83,0.78])
set(text,'fontweight','bold');
legend('Pressure Scanner', 'Transducer', 'Traverse','Location', 'Northeast')

figure(2)
hold on
```

```
plot(data_2675(1:a,1),data_2675(1:a,4))
plot(data_2675(1:a,1),data_2675(1:a,5:9))
plot(traverse_data(:,1)-tshift,traverse_data(:,6),'r')
plot(traverse_data(:,1)-tshift,traverse_data(:,7), 'r')
xlabel('Time (s)')
ylabel('Response')
title('Pressures of Interest')
set(gcf, 'Position', [200 100 800 600])
set(gca,'FontSize',14)
h_xlabel = get(gca,'XLabel');
set(h_xlabel,'FontSize',16);
h_ylabel = get(gca,'yLabel');
set(h_ylabel,'FontSize',16);
h_title = get(gca,'title');
set(h_title,'FontSize',20, 'FontWeight', 'bold');
set(gcf,'Color',[0.82,0.83,0.78])
set(text,'fontweight','bold');
legend('Pressure Scanner','P1','P2','P3','P4','P5', 'Transducer', 'Traverse','Location', 'Northeast')

points=1:300;
figure(4)
hold on
plot(points,Traverse_on_off, points(p:q), data_2675(p:q,5),'r')
plot(points(p:q), data_2675(p:q,6),'r',points(p:q), data_2675(p:q,7),'g')
plot(points(p:q), data_2675(p:q,8),'c', points(p:q), data_2675(p:q,9),'k')
xlabel('Time (s)')
ylabel('Response')
title('Pressure Window Chopping')
set(gcf, 'Position', [200 100 800 600])
set(gca,'FontSize',14)
h_xlabel = get(gca,'XLabel');
set(h_xlabel,'FontSize',16);
h_ylabel = get(gca,'yLabel');
set(h_ylabel,'FontSize',16);
h_title = get(gca,'title');
set(h_title,'FontSize',20, 'FontWeight', 'bold');
set(gcf,'Color',[0.82,0.83,0.78])
set(text,'fontweight','bold');
legend('Traverse','P1','P2','P3','P4','P5','Location', 'Northeast')
```

Appendix B – Labview Data Acquisition

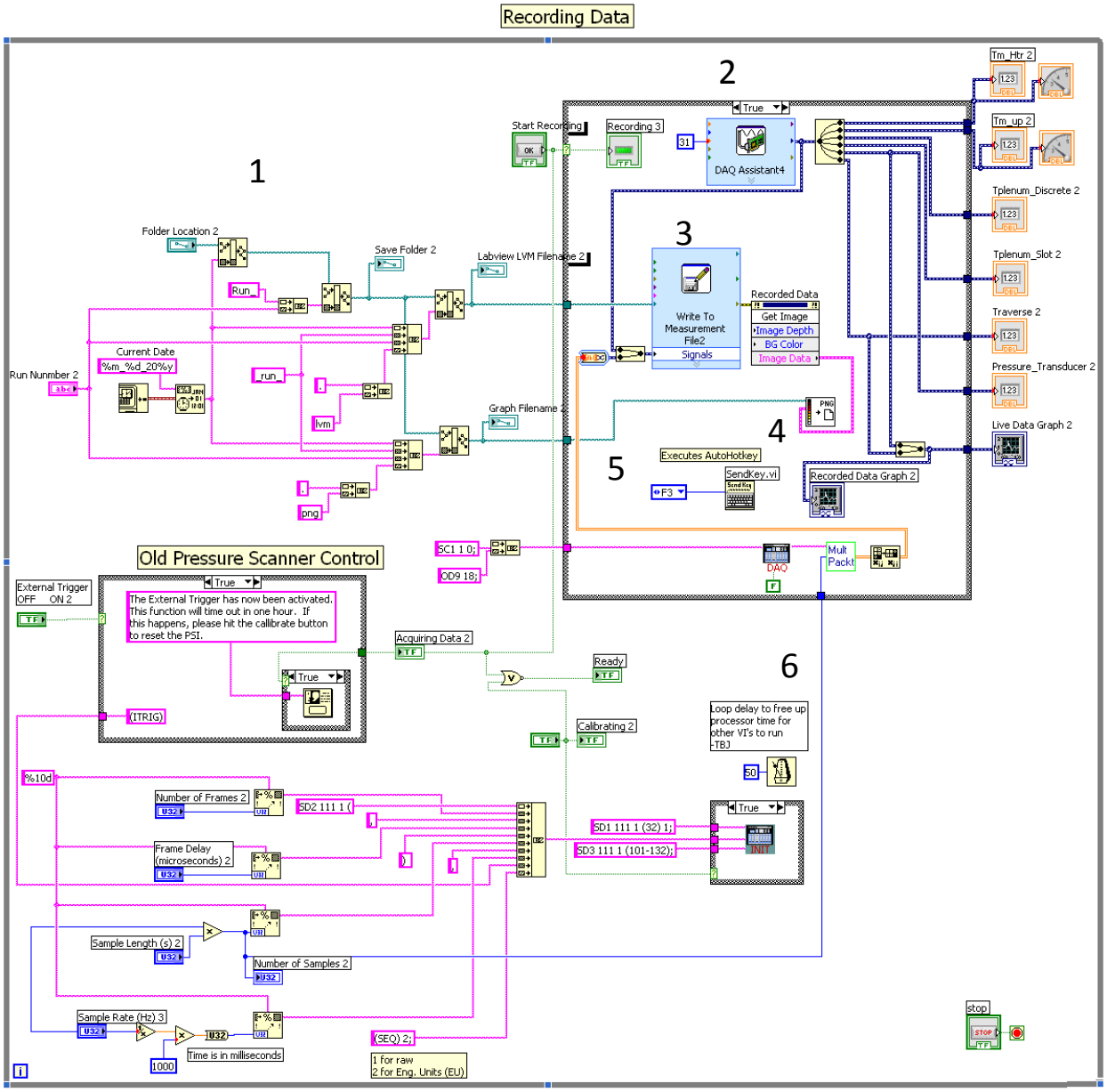

Figure 8.1: Labview Data Acquisition Recording Structure

1) This section of the Labview file creates the file save name output based on the current date and the experimental run number.

2) This is where the NI-DAQ signals are measured.

3) This outputs the measured signals during the 30 second interval of the run and outputs the file as a Labview .lvm file.
4) The tunnel pressure profile and traverse movement signal trace is recorded in a graphical interface and is then saved as an image file for archiving the tunnel performance during the run.
5) The SendKey.vi send the keyboard keystroke of F3 to activate the AutoHotkey command script (Appendix III).
6) The code previously constructed to operate the 8400 PSI system, PSI Data Acquisition Version 4 11_3_08.vi, was copied, modified and integrated into the Labview while loop above to allow for an additional 32 pressure ports from the 48 pressure ports supplied by the Netscanner 98RK.

All outputs produce by the Labview will be saved to the designated location with the first directory being labeled with the current date followed by the subdirectory describing which experimental run was performed.

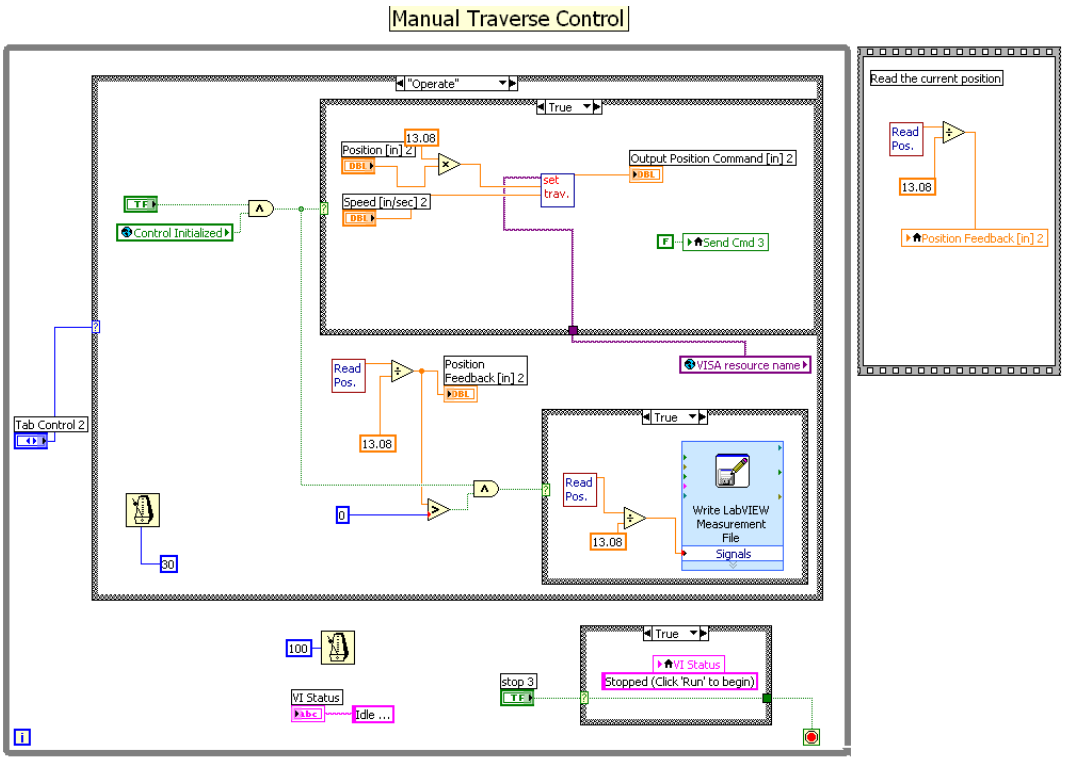

Figure 8.2: Labview Manual Traverse Control Structure

The manual traverse control presented above was a previously developed VI within the lab. This code structure was copied over in the Siemens Labview workspace in order to manually control the traverse for functionality testing before an experiment. However, an additional while loop was created called the "Solenoid Valve Trigger Switch & Traverse Movement and Return." During the film cooling experiments it was imperative that the coolant was not injected before the mainstream was present in the test section. It was ideal that the coolant injection and mainstream flow entered the test section at the same time. Initially this was done by manually turning the power on and off for the solenoid valves. In order to increase experimental precision two physical 10V relays were built to read the output signal from the NI-Daq allowing for the switch between the solenoid valve ejecting into the atmosphere to the plenum and vice versa. The case structure contained a time delay base on the when the "Start Tunnel Run" button was pressed. This was implemented to account for the tunnel ramp up response time.

The second part of the while loop was built to communicate with the traverse. This case structure communicated with "Manual Traverse Control" described above. The values circled in red were hard coded so that when the "Start Tunnel Run" button was pressed" a manually set time delay to account for the tunnel response time, the traverse would move to a maximum distance of 6 inches at a rate of 1 inch per second.

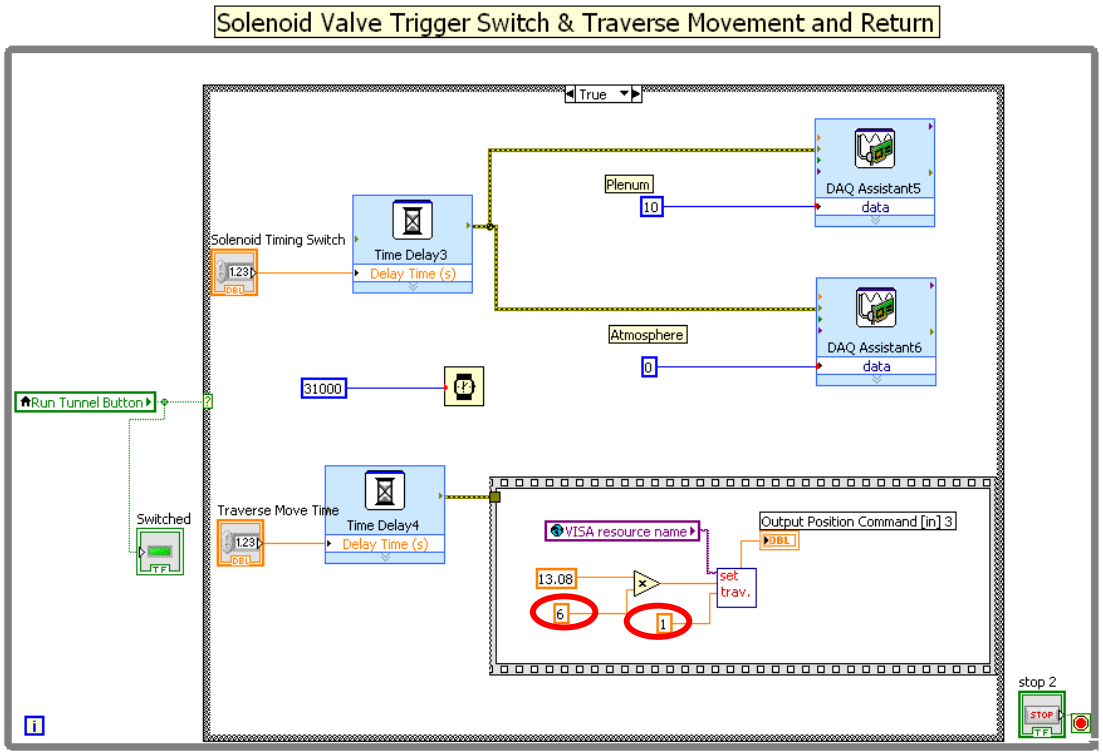

Figure 8.3: Labview Solenoid Valve and Traverse Timing Trigger Control Structure

Once the "Start Tunnel Run" button is pressed the solenoid valve switch and the traverse begins to move after its set time delay. The clock in the case structure Is true for thirty-one seconds. This means that the coolant will be able to enter the test section for 31 seconds until the solenoid valves switch from ejecting into the plenum to ejecting to the atmosphere. The Figure 8.4 below describes the false condition which is responsible for this switch to the original solenoid configuration until the next experiment. Since the traverse moves at 1 inch/sec and

travels a maximum of 6 inches, this means the traverse is in motion for only 6 seconds out of the total 31 seconds. During the rest of the time it sits idle. After the experiment it is necessary to use the “manual Traverse Control” to get the probe back to the start position.

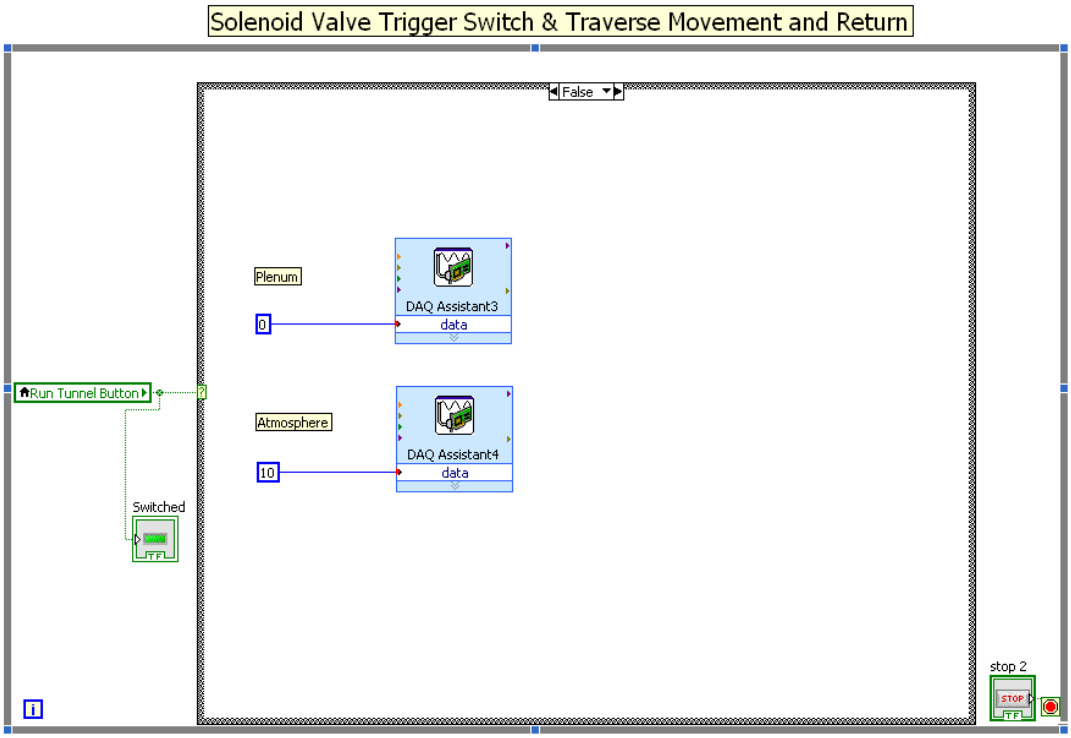

Figure 8.4: Labview Solenoid Valve and Traverse Return to Steady State Control Structure

Appendix C – AutoHotKey Script

The purpose of this code was for increased precision in recording timing between all the data acquisition devices. By pressing the record button (1) in Labview the data being measured by the NI-Daq system would start recording while sending a keystroke command through the SendKey.vi to the FLIR infrared camera software (2) and the Netscanner pressure software (NUSS) (3). This removed the need for multiple computers, personnel, as well as the number or mouse key strokes from 6 to 2 keystrokes, one to start the data acquisition and the other along with the turn of the safety key to start the tunnel run. It is important to note in order for the AutoHotKey script to perform properly the NUSS software (3) must have had record pressed previous to testing in order to highlight the key. This is known when a black dotted highlighting box is present on the button.

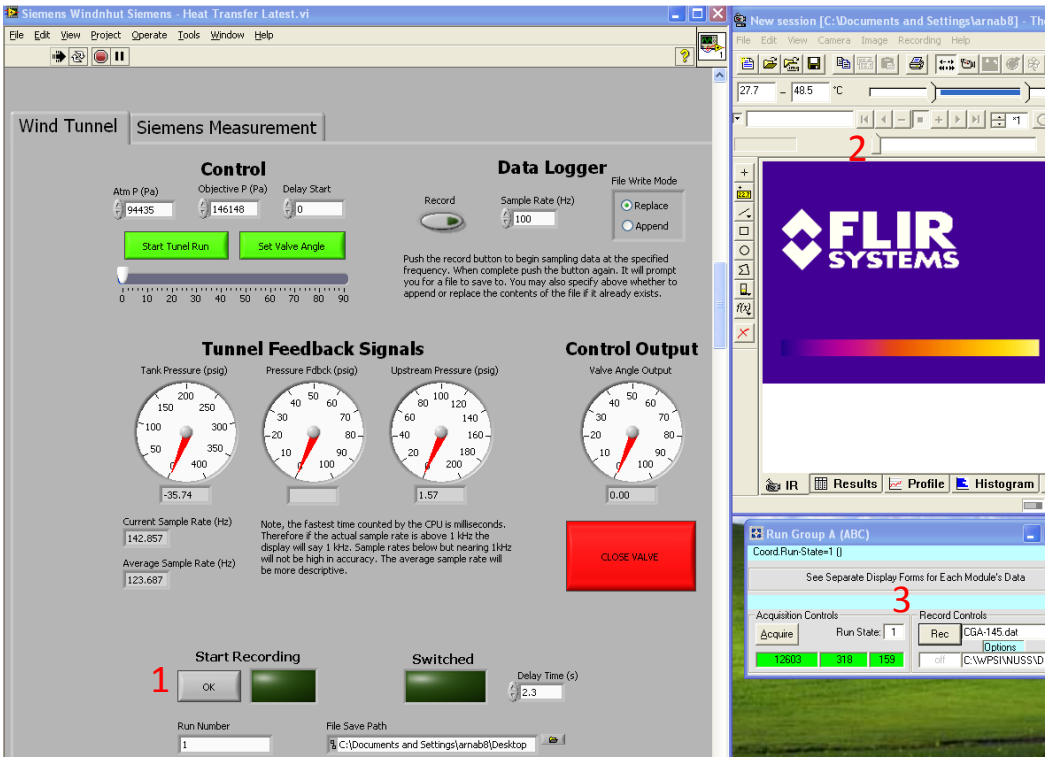

Figure 9.1: Data Acquisition Operating Window (1) Labview Control Panel, (2) FLIR Infrared Control Panel, and (3) NUSS Pressure Scanner Control Panel

% This grabs the current date and formats it with underscores in order to match the image directory location used by the FLIR Software
FormatTime, CurrentDateTime,, MM_dd_yyyy

% By pressing F2 it creates a gui prompt that asks which experimental run is being performed.

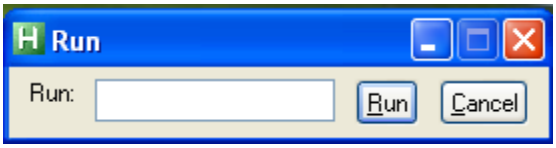

Figure 9.2: AutoHotKey Run Number Input GUI

```
F2::
Gui, Add, Text,, Run:
Gui, Add, Edit, Limit10 vvarRun ym, %varRun%
Gui, Add, Button, ys Default, &Run
Gui, Add, Button, ys, &Cancel
Open=0
If Open = 0
{Open=1
Gui, Show,, Run
return}
Else{
Open = 0
Gui, Cancel
return}
ButtonRun:
Gui, submit
Open = 0
return
```

% By pressing F3 the AutoHotKey program is executed. The F3 command comes from the SendKey.vi in Labview when the Labview record button is pressed. When the program is executed it sends two key strokes to the Netscanner pressure software as well as to the FLIR infrared camera recording software.

```
F3::
```

% The date and the run number previously inputted and formatted is then used to build a string. This is necessary since the image directory used by the FLIR system is based on the date and run number of the experiment. Since this changes daily and with each experiment, this need to be updated accordingly. The reason for this is that the image directory changes the physical window name that the AutoHotKey script needs in order to grab the window and execute the record button.

% This portion of the code grabs the FLIR window and send the F5 command in order to start recording.

```
WinWait, New session [C:\Documents and
Settings\user\Desktop\%CurrentDateTime%\Run_%varRun%\IR] - ThermaCAM Researcher
Professional 2.9,
IfWinNotActive, New session [C:\Documents and
Settings\user\Desktop\%CurrentDateTime%\Run_%varRun%\IR] - ThermaCAM Researcher
Professional 2.9, , WinActivate, New session [C:\Documents and
Settings\user\Desktop\%CurrentDateTime%\Run_%varRun%\IR] - ThermaCAM Researcher
Professional 2.9,
WinWaitActive, New session [C:\Documents and
Settings\user\Desktop\%CurrentDateTime%\Run_%varRun%\IR] - ThermaCAM Researcher
Professional 2.9,
Send, {F5}

% While this portion grabs the NUSS window and send the F5 command in order to start
recording.
WinWait, Run Group A (ABC),
IfWinNotActive, Run Group A (ABC), , WinActivate, Run Group A (ABC),
WinWaitActive, Run Group A (ABC),
Send, {ENTER}

% This tells the program to wait 31 seconds before it stops the recording in both  pressure and
infrared recording software.
sleep, 31000
Similarily, the next two sections send the same commands as before after 31 seconds to stop the
data acquisition.
WinWait, New session [C:\Documents and
Settings\user\Desktop\%CurrentDateTime%\Run_%varRun%\IR] - ThermaCAM Researcher
Professional 2.9,
IfWinNotActive, New session [C:\Documents and
Settings\user\Desktop\%CurrentDateTime%\Run_%varRun%\IR] - ThermaCAM Researcher
Professional 2.9, , WinActivate, New session [C:\Documents and
Settings\user\Desktop\%CurrentDateTime%\Run_%varRun%\IR] - ThermaCAM Researcher
Professional 2.9,
WinWaitActive, New session [C:\Documents and
Settings\user\Desktop\%CurrentDateTime%\Run_%varRun%\IR] - ThermaCAM Researcher
Professional 2.9,
Send, {F5}

WinWait, Run Group A (ABC),
IfWinNotActive, Run Group A (ABC), , WinActivate, Run Group A (ABC),
WinWaitActive, Run Group A (ABC),
Send, {ENTER}
ButtonCancel:
Gui, Cancel
Open = 0
return
```